



저작자표시-비영리-변경금지 2.0 대한민국

이용자는 아래의 조건을 따르는 경우에 한하여 자유롭게

- 이 저작물을 복제, 배포, 전송, 전시, 공연 및 방송할 수 있습니다.

다음과 같은 조건을 따라야 합니다:



저작자표시. 귀하는 원저작자를 표시하여야 합니다.



비영리. 귀하는 이 저작물을 영리 목적으로 이용할 수 없습니다.



변경금지. 귀하는 이 저작물을 개작, 변형 또는 가공할 수 없습니다.

- 귀하는, 이 저작물의 재이용이나 배포의 경우, 이 저작물에 적용된 이용허락조건을 명확하게 나타내어야 합니다.
- 저작권자로부터 별도의 허가를 받으면 이러한 조건들은 적용되지 않습니다.

저작권법에 따른 이용자의 권리는 위의 내용에 의하여 영향을 받지 않습니다.

이것은 [이용허락규약\(Legal Code\)](#)을 이해하기 쉽게 요약한 것입니다.

[Disclaimer](#)

Master's Thesis

A CMOS Indirect Time-of-Flight Sensor with  
Pull-and-Split Charge Transfer Pixel Structure  
for High Depth Resolution

Seunghyun Lee

Department of Electrical Engineering

Graduate School of UNIST

2019

A CMOS Indirect Time-of-Flight Sensor with  
Pull-and-Split Charge Transfer Pixel Structure  
for High Depth Resolution

Seunghyun Lee

Department of Electrical Engineering

Graduate School of UNIST

# A CMOS Indirect Time-of-Flight Sensor with Pull-and-Split Charge Transfer Pixel Structure for High Depth Resolution

A thesis  
submitted to the Graduate School of UNIST  
in partial fulfillment of the  
requirements for the degree of  
Master of Science

Seunghyun Lee

06 / 03 / 2019

Approved by



Advisor

Seong-Jin Kim

# A CMOS Indirect Time-of-Flight Sensor with Pull-and-Split Charge Transfer Pixel Structure for High Depth Resolution

Seunghyun Lee

This certifies that the thesis of Seunghyun Lee is approved.

06 / 03 / 2019

Signature



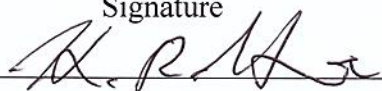
Advisor: Prof. Seong-Jin Kim

Signature



Committee: Prof. Jaehyouk Choi

Signature



Committee: Prof. Kyung Rok Kim

# Contents

<b>Abstract .....</b>	<b>3</b>
<b>Chapter 1. Introduction.....</b>	<b>5</b>
<b>1.1 Motivation.....</b>	<b>5</b>
<b>1.2 Optical Depth Imaging Methods .....</b>	<b>6</b>
1.2.1 Triangulation.....	6
1.2.2 Interferometry .....	6
1.2.3 Time-of-Flight.....	7
1.2.4 Summary of Methods.....	9
<b>Chapter 2. Indirect Time-of-Flight 3D Imaging.....</b>	<b>10</b>
<b>2.1 Principles of Indirect Time-of-Flight 3D Imaging .....</b>	<b>10</b>
2.1.1 Measurement of Modulated Light Signal .....	10
2.1.2 Detection of Signal's Phase through Correlation Function.....	11
<b>2.2 Depth Resolution.....</b>	<b>12</b>
2.2.1 Modulation Frequency .....	12
2.2.2 Demodulation Contrast .....	13
2.2.3 Optical Fill Factor .....	13
2.2.4 Epitaxy Layer Thickness.....	15
2.2.5 Discussion .....	16
<b>2.3 Photonic Devices for Solid-state Imaging .....</b>	<b>17</b>
2.3.1 Charge-Coupled Device (CCD) .....	17
2.3.2 Current-Assisted Photonic Demodulator (CAPD) .....	17
2.3.3 Pinned-Photodiode (PPD) .....	18
<b>Chapter 3. Pinned-Photodiode Demodulation Pixel Design.....</b>	<b>20</b>
<b>3.1 Proposed Pixel Design.....</b>	<b>20</b>
3.1.1 Operation of a 2-tap Demodulation Pixel .....	20

3.1.2 Pull-and-split Charge Transfer Demodulation Pixel Structure .....	21
3.1.3 1 <sup>st</sup> Transfer via Pinning Potential Gradient .....	22
3.1.4 2 <sup>nd</sup> Transfer via 2-tap Transfer Gates .....	23
3.1.5 Demodulation Contrast Improvement using Transfer Gates' $V_{th}$ .....	24
<b>3.2 Performance Comparison through the Measurement.....</b>	<b>26</b>
3.2.1 Experiment Setup.....	26
3.2.2 Signal Intensity Improvement .....	29
3.2.3 Demodulation Contrast of TX Threshold Voltage split.....	29
3.2.4 Performance Measurement with Different Epitaxial Thickness .....	30
3.2.5 Performance Measurement with Different Modulation Frequency .....	35
3.2.6 Demodulation Contrast Measurement with Different Pinning Voltage.....	35
<b>Chapter 4. Summary and Future Work .....</b>	<b>36</b>
<b>List of Figures and Tables .....</b>	<b>38</b>
<b>References .....</b>	<b>41</b>

## Abstract

In recent years, as the demand of various vision applications including robot vision and VR/AR systems increases, many Time-of-Flight (TOF) sensors are developed and commercialized which can measure depth not only with cm to mm-scale depth resolution in a few meters range, but also maximized target range over 100m. As the history of color image sensor has shown the direction, TOF sensors' development would be continued towards pixel scaling to have spatial resolution while keeping the depth resolution and the cost.

Then, what kind of applications can be possible through 3D imaging? First, an automotive application can be an example. Imagine the situation of driving a car in a dark environment, and we almost can't see the people around. With 3D imaging technology, the depth perception is possible in the dark, as well as the detection of an object. The next one is the user interface. There are many SF movies with scenes that the actor controls the device or computer with his or her gestures, not using a conventional keyboard, or mouse. This can be possible with the person's gesture recognition through 3D imaging. Last one is the robot vision. With the sensors on top of the robot, the depth recognition can help the machines to interact with environments around it. For example, the robot can perceive the obstacles around it, and they reach the destination without colliding other objects, such as bookshelf, tables, or people moving around.

To realize these applications, there are many 3D imaging techniques. Triangulation, time of flight, and interferometry can be an example. Triangulation is roughly composed of two categories; one is structured light and the other is stereo vision. Structured light shoots the patterned light, and the reflected light is received onto two or more sensors, and the pattern's difference among them gives the depth output. The stereo vision works as same as human eyes. This can also detect depth through the difference among sensors' output through the calculation of trigonometric functions, except this one does not use the active light. There are two big disadvantages of the triangulation technique; one is the number of sensors, which needs at least 2 sensors, and the other one is the computational power, which is higher than other methods.

The next one is the time-of-flight technique. The time-of-flight basically measures the round-trip time of the illuminated light until it comes into the sensor. As the name states, the DTOF measures the time directly, and ITOF measures the phase delay. DTOF uses a single photon avalanche diode (SPAD) for its photonic device, and ITOF can use a photogate [1], pinned photodiode, and current-assisted photonic demodulator (CAPD). The TOF technique's strength is that it needs only 1 sensor for depth detection. Due to the strength, this research is focused on ITOF method with pinning photodiode structure.

The interferometry detects distance using optical coherence of the illuminated light and reflected light, thus micrometer to nanometer scaled depth detection can be done, but the maximum



distance is too short, and the system is too bulky, so it is used for scientific use.

Various factors affect Indirect Time-of-Flight (I-TOF) sensor's depth resolution performance. From the pixel's perspective, Quantum Efficiency (QE), and modulation frequency are the most critical factors among them. Since most of the TOF system uses near-infrared (NIR) region as its light source for end users' eye convenience, silicon's low QE in this wavelength can cause a low photo-generated signal comparing to emitted light power [2], resulting low depth resolution. Thick epi-layer can solve this problem, however, there is a trade-off between the epi-layer thickness and the maximum modulation frequency [3].

It is known that the depth resolution becomes favorable as the modulation frequency increases since the I-TOF sensor detects the depth result from the phase difference between the emitted light and the received light, and speed of light is always fixed. However, epi-thickness limits maximum modulation frequency since the electrons must be transferred through longer distance to reach the designated FD within the limited time interval to detect the phase difference caused by the target object's actual distance from the sensor.

In this research, the proposed pixel has pull-and-split charge transfer using different n-doping profile inside pinned photodiode (PPD) which generates lateral electric field to push the photo-generated electrons towards designated FD. The unit PPD is composed of two regions, one is lightly doped with Arsenic which has low pinning potential, and the other is highly doped near the FD to have higher pinning potential, therefore, lateral electric field can be generated. The lightly doped area is designed to have wide area to get a high fill factor, and the highly doped area is designed to have minimal distance between two TX gates. The two TX gates' distance is carefully designed to have proper lateral e-field through TCAD simulation. Through this structure, the electrons are transferred towards the highly doped area via pinning potential gradient, and the TX gates transfer electrons inside highly doped area. Unit pixel pitch is 14.4 $\mu$ m with the fill factor of about 48% without a microlens. It is composed of 8 PPDs to reduce the electrons' lateral travel distance. This chip is fabricated with a 0.11 $\mu$ m CIS process with the minimal change from conventional CMOS Image Sensor technology. In addition, the implementation and measurement of I-ToF sensor are reported with different parameters such as epi-layer thickness, different PPD structures, and PPD's n-dose for performance comparison.

# Chapter 1. Introduction

---

## 1.1 Motivation

Until now, the camera has shown us the 2-dimensional images. Therefore, the development of image sensor has paved the way towards the true color imaging, high dynamic range (HDR), while increasing the image's spatial resolution with the scaling of pixel size. However, as the other technologies such as human-computer interaction, or robotics, and internet of things (IoT) grow up, the demand for additional information from sensor has also been increased, the depth information as the one of the most demanded. Therefore, the sensor's dimension of perceiving the world is not limited to 2-dimension through the development of 3D imaging technology.

Retrieving additional depth information from an image sensor has many advantages in case of applications. The automotive application can be an example. Recently, the car companies are trying to develop the autonomous driving system implanted to a car. To realize this application, the car itself should be aware of any obstacles and objects nearby it, even in the high-speed driving in a highway. The big electric car company, TESLA, has launched the model X with the autopilot function included in 2015, and it has been produced until now. Seeing it in detail, there are many sensors not only frontside and backside of the car, but all around the car, so that there is no blind-area. Many types of sensors are used, such as the radar and ultrasonic. The depth information retrieved from these sensors are collected and the computer inside determines the speed and direction of the car.

Another application is robot vision. Like the autonomous driving application, the depth detection sensor can also be applied on robots. One example can be the information robot Airstar, done by Naverlabs. This robot is dispatched to the Incheon National Airport and does its job by moving all around the airport and gives other passengers and visitors a helping hand, for example, by guiding to their destination when they are lost. In this application, the robot should be aware of obstacles and people moving around by multiple depth sensors.

Only two of the examples are shown above, but these examples truly show the possibility of using depth sensors for many applications. However, these kinds of applications cannot be done without the accurate depth perception 3D imaging sensor as its hardware. Therefore, the development of 3D imaging technology further will pave the way towards the new world via novel technologies.

## 1.2 Optical Depth Imaging Methods

In this chapter, the methods for optical depth imaging is discussed. There are many techniques for the sensors to perceive the environment, triangulation, interferometry, and time of flight. The principles of each technique are roughly discussed, and they are compared each other.

### 1.2.1 Triangulation

The triangulation is based on the geometrical properties of triangles, and this is the way how people perceives depth, or distance. It is known that triangles have three points on it, so if we know the position of two points and the distance between them, measuring the angles from these two points to the target object can generate triangle, and simple calculation gives us the object's distance [4]. This situation is illustrated in figure 1.1.

The triangulation method can measure distance from mm-scale to km-scale, which is one of the strengths of this method. However, to achieve proper depth resolution with appropriate maximum distance scale, large system is needed since the triangle drawn in figure 1.1 should be large. In addition, the measurement should be done in two points, which states that at least two sensors are needed.

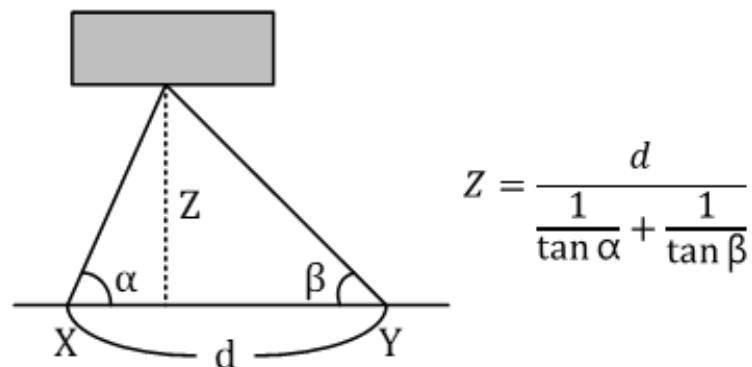


**Figure 1.1** The triangulation diagram and depth formula. Two observation point are needed, X and Y.

### 1.2.2 Interferometry

The interferometry utilizes the electromagnetic waves' interference. It is composed of coherent light source, beam splitter in the middle, mirror, detector, and the object. The diagram of interferometry, especially Michaelson interferometer is drawn in figure 1.2. As the light source illuminates the light, the beam splitter splits incoming light into two direction, one is transparent direction and the other is reflected direction, and they form the right angle. The one which goes to the reflected direction comes back after hitting the mirror, and is transparent towards vertical direction, reaches the detector. The other light, which was transparent in first interaction, hits the object and comes back to the beam splitter. This time, the light is reflected towards the detector side, and reaches

the detector.

Based on this situation, the two incoming lights are integrated by the detector, and the measurement of these two waves' interference makes depth detection of the object possible. This method is good for detecting very small displacement of the object, making its depth resolution from  $\mu\text{m}$  scale to  $\text{nm}$  scale. However, the maximum detectable range is very limited, a few tens of  $\text{cm}$  scale. The other drawback is that the system complexity is too high. It needs many optical devices calibrated and fixed accurately, and the accurate laser illuminator is needed. These strengths and drawbacks made this application widely used in scientific and industrial applications.

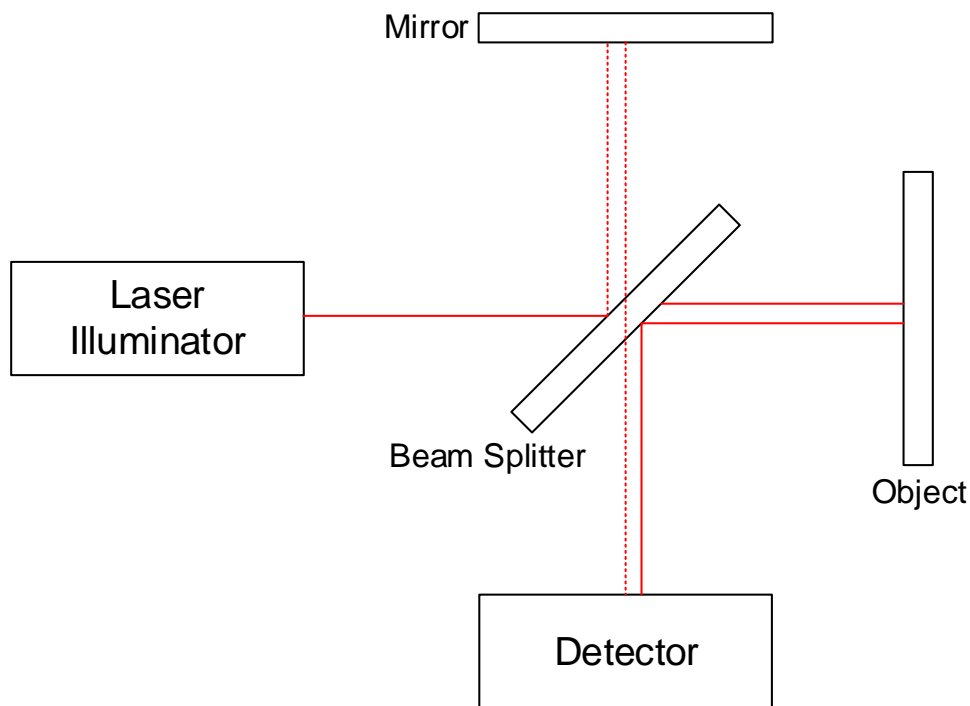


**Figure 1.2** The Michaelson Interferometer. The lights are described in dashed one and solid line, to distinguish two paths of beam-splitter's output.

### 1.2.3 Time-of-Flight

The time of flight basically measures the round-trip time of the illuminated light until it comes into the sensor. This method is composed of two types, one is the Direct Time-of-Flight (DTOF), and the other one is Indirect Time-of-Flight (ITOF). As the name states, the DTOF measures the time directly, and ITOF measures the round-trip time in indirect way, phase delay. DTOF uses a single photon avalanche diode (SPAD) for its photonic device, since the accurate pulse input is needed for measuring the round-trip time directly, but making SPAD with good performance is hard, and scaling of this device is also hard to achieve. Another burden of DTOF is that the high-speed operation of the circuit is required to measure the time-of-flight directly. Since the speed of light is as fast as  $300,000\text{km/s}$ , the pulse must be detected in sub-nanosecond scale for reasonable depth

accuracy. In contrast, ITOF can use photogate, pinned photodiode, and CAPD. Since the ITOF measures the distance in an indirect way, conventional photosensitive devices can be used for its photonic device. The TOF technique's strength is that it needs only 1 sensor for depth detection, and the system configuration is not bulky, comparing to the other methods. Due to the strength, this research is focused on ITOF method.

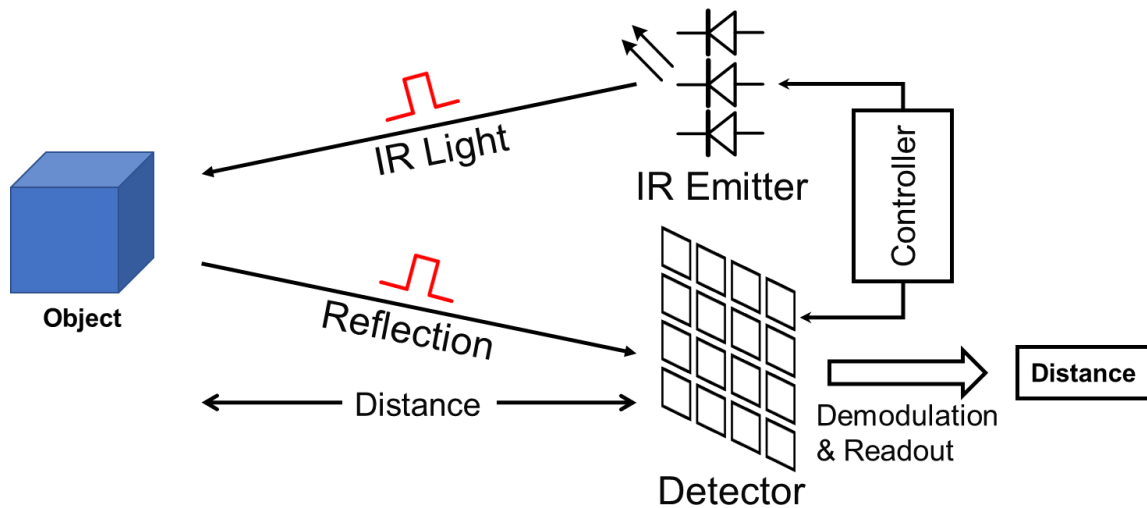


**Figure 1.3** The Time-of-Flight method diagram. It is composed of IR emitter and detector, and the detector reads the round-trip time of the emitted light.

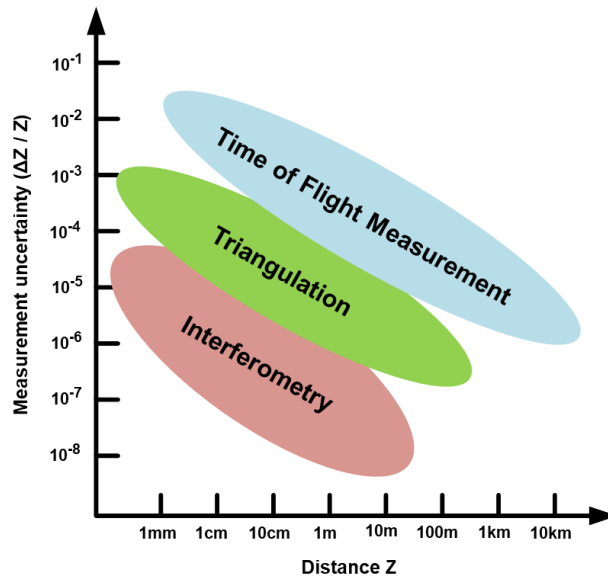


**Figure 1.4** The comparison of three methods based on target distance and the measurement uncertainty [5].

### **1.2.4 Summary of Methods**

The characteristics, and rough principles of each method are described above. The target specifications of these methods are drawn in figure 1.4. Although interferometry has best accuracy among these three methods, due to the limitations of maximum detectable distance and costly system, this method is not selected for this research. Next, for the triangulation's case, since this method is good for measuring various ranges, but this also has bulky system based on the target distance, and since this system needs 2 or more sensors, it is also excluded, the time-of-flight method, especially the Indirect Time-of-Flight is selected for this research.

## Chapter 2. Indirect Time-of-Flight 3D Imaging

### 2.1 Principles of Indirect Time-of-Flight 3D Imaging

#### 2.1.1 Measurement of Modulated Light Signal

The basic principles of Indirect Time-of-Flight (I-TOF) 3D imaging are presented in this chapter. The Time-of-Flight 3D imaging is roughly composed of 3 components, optical emitter, light receiver (i.e. lens), and photonic detectors. Since silicon's absorption coefficient is relatively high around 400 – 1000nm (visible to near infrared) wavelength range, optical emitter in this system can use this spectrum of light. For performance, green color wavelength is useful since silicon's absorbance at this range is higher than near infrared (NIR) range. However, in the users' perspective, visible light onto users' eye may be interruptive, especially spatial range detection, i.e. 2D scene depth detection, and sometimes it can also be harmful in case of shorter wavelength and high illumination power. Therefore, for both eye safety issue and users' convenience, NIR range is normally preferred for the Indirect Time-of-Flight system's optical illuminator's wavelength.

As for an operation of TOF system, 1 or multiple optical emitters emit light towards to the object of interest, and the reflected light is focused and collected with the lens, thus the photonic detector can receive light information onto its surface. The received light's signal is demodulated and interpreted as distance data through the detector and its periphery circuits.

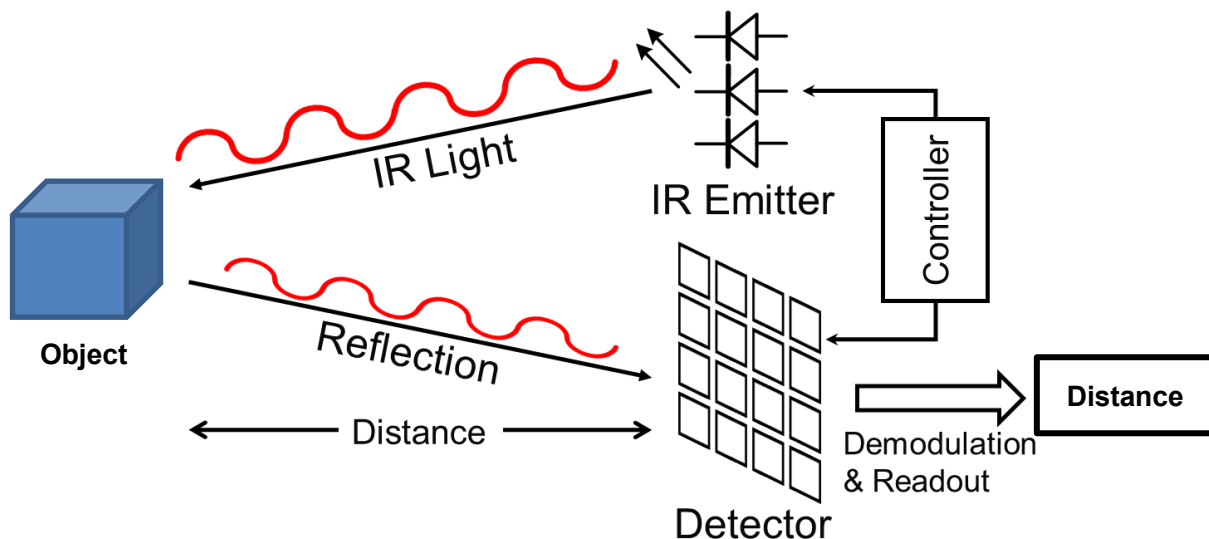


**Figure 2.1** Basic principle of Indirect Time-of-Flight 3D imaging system.

The main difference between Direct Time-of-Flight (D-TOF) and Indirect TOF is information on the interest. Unlike Direct TOF 3D imaging, the I-TOF detects the phase difference between illuminated light and detected light which is reflected and comes back from the target object. Therefore, the light illuminator and detector is synched in the I-TOF system for the proper operation. Figure 2.1 shows the basic principle of I-TOF system.

## 2.1.2 Detection of Signal's Phase through Correlation Function

We know that the light's phase delay is proportional to the target objects' distance from the IR emitter. The I-TOF utilizes this phase difference between emitted light and received light to get distance information. The correlation function can be used to calculate the distance by using two signals. The definition of correlation function is as follows [6]:

$$\text{corr}(s(t), g(t)) = \lim_{T \rightarrow \infty} \frac{1}{T} \int_{-\frac{T}{2}}^{\frac{T}{2}} s(t)g(t + \tau) dt \quad \text{Equation 2.1}$$

Also, original modulation signal  $g(t)$  and received light signal  $s(t)$  is defined as follows:

$$g(t) = \cos(\omega t), \text{ and } s(t) = 1 + a \cos(\omega t - \theta) \quad \text{Equation 2.2}$$

Calculating correlation function between  $g(t)$  and  $s(t)$ , i.e., cross correlation gives:

$$\begin{aligned} \lim_{T \rightarrow \infty} \frac{1}{T} \int_{-\frac{T}{2}}^{\frac{T}{2}} s(t)g(t + \tau) dt &= \lim_{T \rightarrow \infty} \frac{1}{T} \int_{-\frac{T}{2}}^{\frac{T}{2}} [1 + a \cos(\omega t - \theta)][\cos(\omega t + \tau)] dt \\ &= \frac{a}{2} \cos(\omega t + \theta) = C(\omega t) \end{aligned} \quad \text{Equation 2.3}$$

Since we need  $\theta$  from Equation 2.3., substitute  $C(\omega t)$  with  $\omega t = 0^\circ$ ,  $\omega t = 90^\circ$ ,  $\omega t = 180^\circ$ ,  $\omega t = 270^\circ$  gives followings:

$$\begin{aligned} C(0^\circ) &= \frac{a}{2} \cos(\theta) & C(90^\circ) &= -\frac{a}{2} \sin(\theta) \\ C(180^\circ) &= -\frac{a}{2} \cos(\theta) & C(270^\circ) &= \frac{a}{2} \sin(\theta) \end{aligned} \quad \text{Equation 2.4}$$

Thus, the phase difference  $\theta$  from Equation 2.4 is calculated by followings:

$$\tan(\theta) = \frac{C(270^\circ) - C(90^\circ)}{C(0^\circ) - C(180^\circ)}, \text{ therefore } \theta = \arctan\left(\frac{C(270^\circ) - C(90^\circ)}{C(0^\circ) - C(180^\circ)}\right) \quad \text{Equation 2.5}$$

Finally, the distance from the phase difference is:

$$\text{Distance} = \frac{c}{4\pi f} \arctan\left(\frac{C(270^\circ) - C(90^\circ)}{C(0^\circ) - C(180^\circ)}\right) \quad \text{Equation 2.6}$$

where  $c$  is speed of light, and  $f$  is modulation frequency.



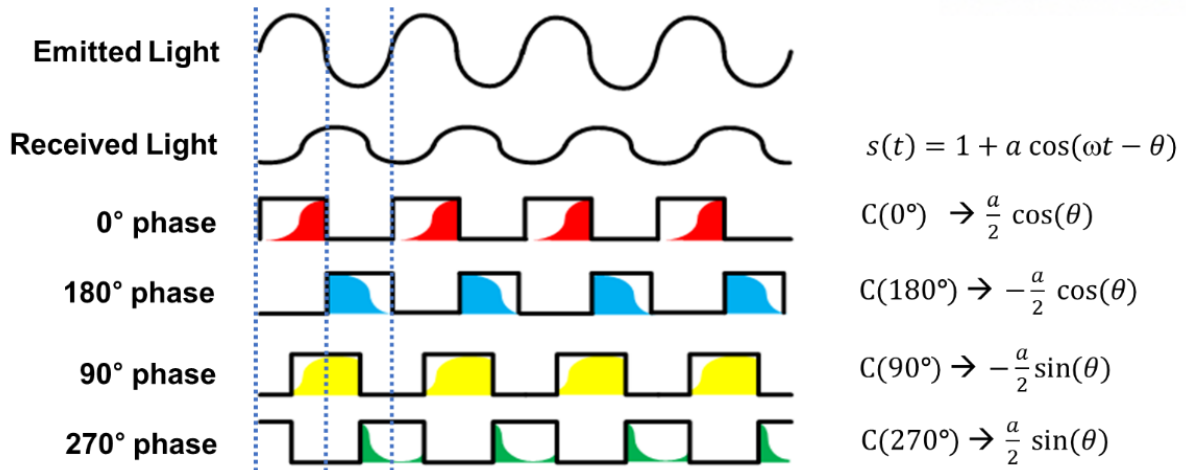


Figure 2.2 Sampling of received light in an Indirect Time-of-Flight sensor.

## 2.2 Depth Resolution

The depth resolution of I-TOF is known as [7]:

$$\sigma_R = \frac{c}{4\pi f_{mod}\sqrt{2}} \cdot \frac{\sqrt{A_{sig} + Ambient}}{C_{demod}A_{sig}} \quad \text{Equation 2.5}$$

where  $f_{mod}$  is modulation frequency,  $C_{demod}$  is demodulation contrast, and  $A_{sig}$  = signal intensity.

### 2.2.1 Modulation Frequency

The modulation frequency indicates the frequency of the modulated light source. A lower modulation frequency can give us theoretically longer maximum detectable distance since the phase delay we can detect becomes larger for the low modulation frequency. However, the maximum detectable distance is interpreted from the phase delay of received light, 1 degree of phase delay indicates longer distance step, thus the resolution of the detectable distance is decreased.

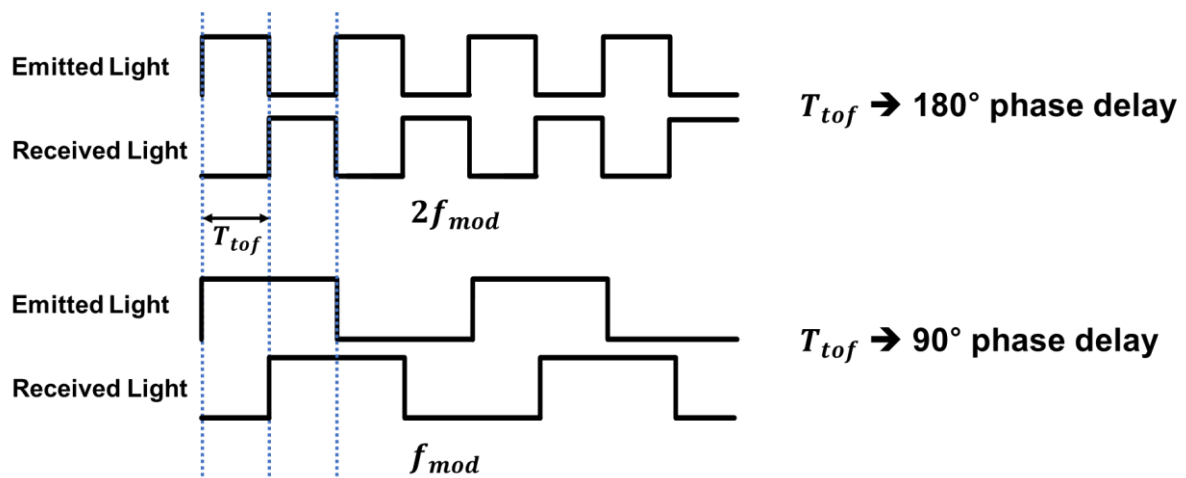


Figure 2.3 Timing diagram of the same time delay with different modulation frequency.

Figure 2.3 shows the different modulation frequency  $f_{mod}$  and  $2f_{mod}$  with the same time delay of received light, i.e., the target object's distance is same. For the low frequency case, the  $T_{tof}$  is interpreted as 90-degree phase shift, but the higher frequency case, the  $T_{tof}$  is interpreted as 180-degree phase shift at the expense of maximum distance. Therefore, for the higher depth resolution, the pixel should operate in high modulation frequency. Most of the I-TOF pixels use the modulation frequency is in a range of few 10 MHz and sometimes 100 MHz or more at the maximum. For the pixels to operate in such high frequency, the pixel should have high demodulation contrast, which is explained below.

### 2.2.2 Demodulation Contrast

Demodulation contrast is the demodulation pixel's performance parameter which indicates the accuracy of the modulated input light signal into different phases, i.e.  $0^\circ$  and  $180^\circ$  phase. This value is defined as following [7]:

$$C_{demod} = \frac{2\sqrt{(A_0 - A_{180})^2 + (A_{90} - A_{270})^2}}{A_0 + A_{90} + A_{180} + A_{270}} \quad \text{Equation 2.6}$$

where  $A_0$ ,  $A_{90}$ ,  $A_{180}$ ,  $A_{270}$  means the collected light signal intensity for each phase. The demodulation contrast's range is from 0 to 1, and we can say the pixels' demodulation performance is good when this value is large, ideally reaching to 1. Through this value, we can compare different pixels' inherent demodulation performance.

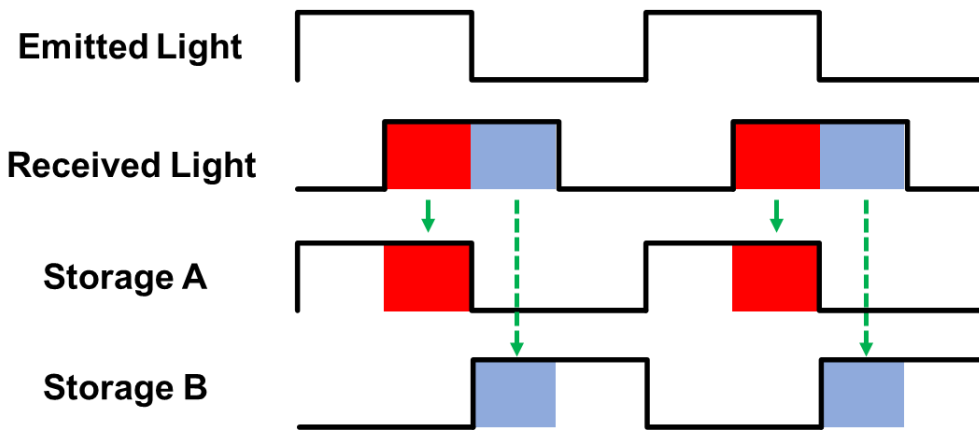


**Figure 2.4** Timing diagram of demodulation sequence. Demodulating received light and store them on different storage is the key performance for demodulation.

### 2.2.3 Optical Fill Factor

The optical fill factor indicates the ratio of a unit pixel's total area and photodiode's effective light receiving area. Therefore, this value lies on from 0 to 1, and the microlens on top of the pixel can increase the effective optical fill factor by focusing the scattered light onto the pixels' light receiving

area, photodiode. Without the microlens, some of the incoming light may not be able to reach towards the light sensitive area due to in-pixel routings, poly gates, etc., thus microlens helps the pixel to increase the effective optical fill factor.

$$\text{Optical fill factor} = \frac{\text{Pixel's light sensitive area}}{\text{Total unit pixel area}} \quad \text{Equation 2.6}$$

As the optical fill factor is increased, the pixel can receive the amount of light more within the same unit pixel pitch, therefore, this can give better SNR. In I-TOF case, since it needs active illumination, i.e. the IR emitter emits light onto the target objects and scene, and since the light's intensity is inversely proportional to the square of light travel distance, the situation that sees the object far from the sensor is much more critical than the normal color image sensor's case. Therefore, the pixel's optical fill factor should be maximized to get enough photoelectrons generated by illuminated IR light.

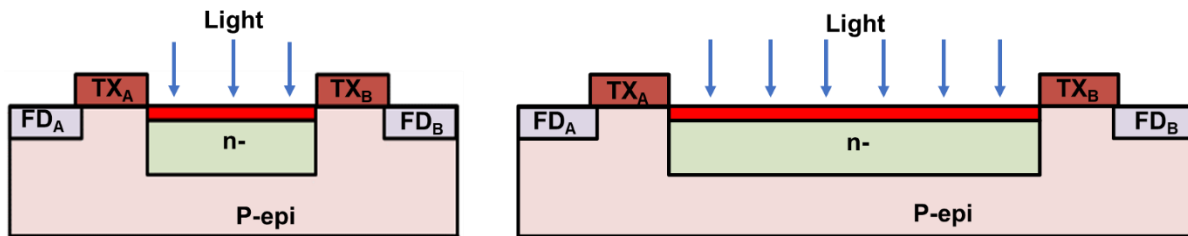


**Figure 2.5** Two pixels which have different fill factor. The size of photosensitive area defines the sensitivity to incoming light, thus gives high SNR.

However, when the photodiode's area is designed too large to have high sensitivity, it may cause bad demodulation contrast. Normally, the I-TOF pixels have at least two storage nodes called floating diffusion (FD), and they are connected to the photosensitive area via poly gates. Proper demodulation indicates proper transfer of photo-generated charge in limited time, defined by modulation frequency. Inside photodiode, most of the photoelectrons are transferred by drift and diffusion. The multiple transfer gates (TX<sub>A</sub> and TX<sub>B</sub> in figure 2.5 and 2.6) causes e-field onto photodiode to pull the photoelectrons when they are turned on. However, when the distance from these two TX gates increases, the e-field generated by their voltage is decreased, thus the transfer efficiency is drastically decreased. This situation is described in figure 2.6.

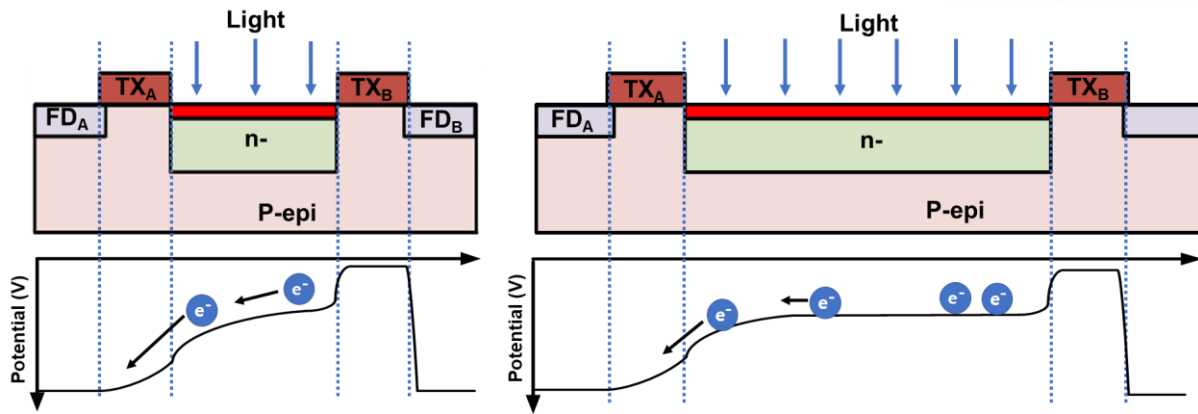


**Figure 2.6** Large fill factor can have more light signals, but transfer efficiency is decreased. This may cause the decrease of the charge transfer efficiency, decreasing demodulation contrast.

## 2.2.4 Epitaxy Layer Thickness

Another way to increase SNR is the use of a thicker epitaxial layer. Epitaxial layer is a thin layer of single-crystal silicon over a silicon substrate, which is commonly done with the chemical vapor decomposition process. In circuit's perspective, epitaxial layer has many advantages, including improvements of bipolar devices' performance, prevention of latch-ups in CMOS circuits. In addition, for photodiodes, thick epitaxial layer gives better photosensitivity. As mentioned in 2.2.3, large fill factor can give higher photosensitivity, but it can decrease the pixel's charge transfer efficiency, therefore, demodulation performance is also decreased. In addition, a bigger unit pixel's size gives lower spatial resolution, therefore a low image resolution is produced as a sensor's output, which is not preferred.

To resolve this problem, epitaxial layer of proper thickness for photodiode can be fabricated to increase the pixel's SNR. However, too thick epitaxial layer may cause pixel-to-pixel crosstalk problem, which is not preferred especially in color image sensor.

In addition, from the I-TOF pixel's perspective, too thick epitaxial layer can also incur charge transfer efficiency problem, the same problem as the optical fill factor of the pixel. Figure 2.7 shows the situation. Since I-TOF system uses NIR wavelength for illumination, and NIR's absorption length in silicon is about a few micrometers, which is longer than other visible light wavelengths, most of the photo-generated charges invoked by I-TOF's illuminator are located deep inside of photodiode towards substrate. In addition, when thicker epitaxial layer is applied, additionally generated photoelectrons by the layer have longer travel distance than other electrons, and weaker e-field is applied to this area, so they may not be transferred in limited time. Therefore, they may be transferred to the wrong storage node, resulting a wrong depth image.

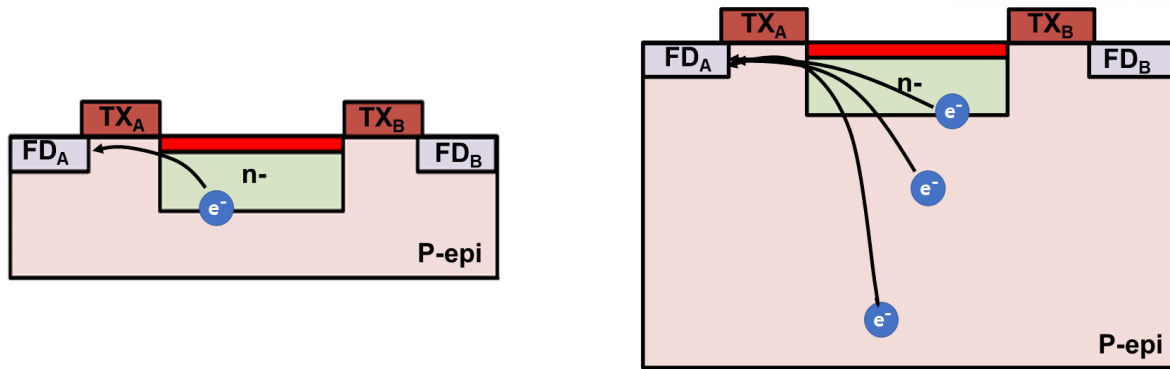


**Figure 2.7** Thicker epitaxial layer may increase photosensitivity of photodiode, especially in longer wavelength. However, since some of the photoelectrons have longer travel distance to reach the destination, FD nodes, and e-field generated by TX gates is much weaker, so charge transfer efficiency is decreased.

### 2.2.5 Discussion

The factors which can affect the I-TOF pixel's depth resolution performance is discussed. Pixels which operates in high modulation frequency can give a high resolution of phase delay, thus depth detection with high accuracy can be performed, at the expense of maximum detectable range. However, if the pixel's demodulation contrast is not high enough, then the pixel cannot detect accurate depth even though the illumination light has high modulation frequency. The demodulation contrast is the pixel's performance parameter which indicates the efficiency of demodulation at a certain modulation frequency. It is affected by photo-generated charges' transfer efficiency, so proper methods should be applied to increase transfer efficiency. The optical fill factor is directly related to the amount of incoming light. The bigger pixel can receive more light, resulting higher SNR. However, if the pixel becomes too big, it can incur low image resolution, and lower charge transfer efficiency due to charge's longer travel distance and weakened e-field. The usage of a thicker epitaxial layer is discussed to enhance SNR within a same pixel size. Since I-TOF uses NIR illumination, this can enhance effective SNR more than visible light's case. However, this also suffers from lowering demodulation contrast due to longer travel distance, the similar problem as in a bigger pixel's case. Within this trade-off relationship, the optimal pixel design is needed for high depth resolution.

## 2.3 Photonic Devices for Solid-state Imaging

### 2.3.1 Charge-Coupled Device (CCD)

Charge-coupled device, known as CCD, has been widely used for solid-state image sensing since its invention in 1970 [8]. It is composed of photodiodes and multiple transfer gates, called CCD gates. Same as the other imaging devices, photodiode works as collector of incoming light, and each transfer gates located next to photodiode drives photoelectrons beneath it. The chains of CCD gates transfer electron itself towards the chip's output. To avoid Si-SiO<sub>2</sub> not to be interrupted during charge transfer, buried channel implant is applied beneath the CCD gates. Since the CCD's operation transfers photoelectron itself, the charge transfer efficiency is very important, especially spatial resolution is high. For example, let CCD's spatial resolution is 1920 x 1080, and the first row of the image is read out first in row-by-row readout operation. To transfer 1<sup>st</sup> row's photoelectrons towards the end of photosensitive area, 1080 times of transfer should be done. Even the transfer efficiency is 99.99999%, i.e., 1 electron among a million electrons lost, multiplying 1080 times gives 0.99989 %, meaning that achieving accurate readout while achieving a high spatial resolution is very hard. In addition, to achieve nearly perfect charge transfer efficiency, perfect silicon crystal is needed, making it expensive.

### 2.3.2 Current-Assisted Photonic Demodulator (CAPD)

Current-Assisted Photonic Demodulator was invented in 2005 [9]. As the name states, the current applied on the pixel drives photo-generated electrons towards the detection node. The alternating current is applied onto two guide nodes which is placed directly onto p-substrate ( $V_{\text{guide1}}$  and  $V_{\text{guide2}}$  in figure 2.9). The e-field generated by this alternating current produces e-field even deep inside of photosensitive area, thus demodulation of high frequency is possible with the increased SNR through thick epitaxial layer. However, since the current is applied directly onto substrate, if the resistivity of substrate is low, and the potential difference between two guide nodes is high, it can cause large current consumption, generating heat inside, thus high thermal noise. Moreover, when the pixel pitch is scaled down, then the distance between two guide nodes is also scaled down. This will incur the e-field's decrease in deep areas of p-substrate, therefore demodulation efficiency at thick epitaxial layer decreases, so pixel size scaling is difficult to achieve while keeping demodulation performance.

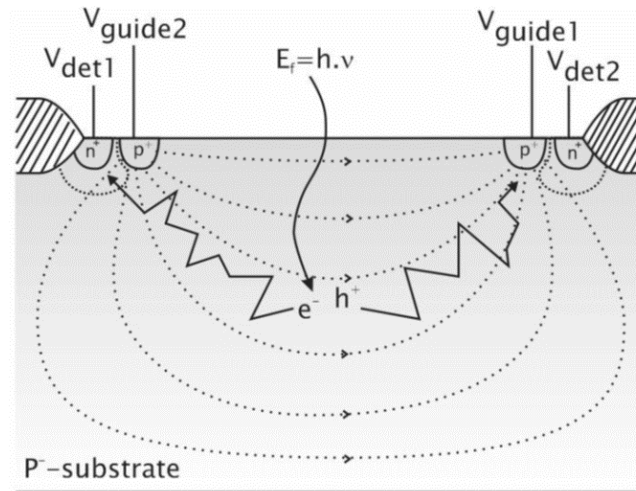


**Figure 2.8** Structure of CAPD.  $V_{guide1}$  and  $V_{guide2}$  works as nodes to apply demodulation current, and  $V_{det1}$  and  $V_{det2}$  are detection nodes.

### 2.3.3 Pinned-Photodiode (PPD)

Since the invention of pinned photodiode by Nobukazu Teranishi in the early 1980s [10], it has become a winning solution for the photon-detecting device in a CMOS image sensor. Pinned photodiode has a structure drawn in Figure 2.10 [11]. Photodiode's n layer is placed on p-substrate, and thin p+ layer is placed on top of n layer. This thin p+ layer is called pinning layer. With the p-n junction placed back-to-back structure, photodiode layer's voltage is 'pinned' to certain voltage, so this voltage is called pinning voltage.

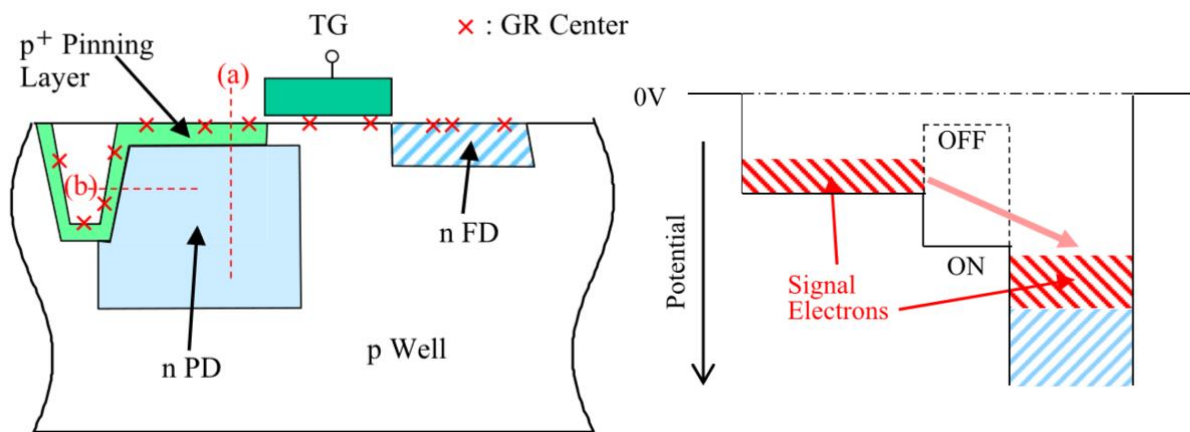


**Figure 2.9** (left) The structure and (right) the potential diagram of pinned photodiode.

This structure has two of the most important advantages, 1) complete charge transfer and 2) effect of p+ pinning layer. First, complete charge transfer means all the photoelectrons generated

inside photodiode is fully transferred into FD node in the limited time interval. Since the highest potential (the potential when photodiode is empty of photoelectrons) inside pinned photodiode is ‘pinned’ at proper voltage that is lower than TX’s on voltage, the photoelectrons can be fully transferred towards FD, making no image lag.

The second advantage, the effect of p<sup>+</sup> pinning layer on top of photodiode. The dark current is the generated current inside PD even when there is no incoming light. The dark current can be generated in many places inside PD, but Si-SiO<sub>2</sub> interface is one of the most critical part among them. In this situation, p<sup>+</sup> pinning layer on top of PD helps these electrons generated by non-light source to recombine before they come inside of PD, making low dark noises.

In I-TOF application, the PPD’s complete charge transfer is one of the most important features. Charge transfer characteristics of the photon detection device is directly related to the demodulation contrast of I-TOF pixel performance, so the use of PPD as I-TOF pixel has high potential. Not only for the transfer characteristics, but also the low dark noise effect can be helped. Since the light intensity is reduced in the square of travel distance, if the target object is a few meters away from the I-TOF sensor, then the reflected IR light is significantly decreased, making low SNR. By reducing dark noise sources using PPD structure can help I-TOF sensor to have higher SNR.



---

## Chapter 3.

# Pinned-Photodiode Demodulation Pixel Design

---

### 3.1 Proposed Pixel Design

#### 3.1.1 Operation of a 2-tap Demodulation Pixel

Demodulation pixel has many variations according to the number of storage nodes (Floating Diffusion, FD, or tap). The pixel normally has at least 2 taps for demodulation. Otherwise, 3 or more taps can be used as well. Multiple taps with the reduced duty cycle of illuminated light can be used for extending maximum distance or reducing ambient light illumination effect by storing background light only inside one of the taps and subtracting that voltage from other storage nodes which have reflected light's information.

Among these multiple selections for the number of taps, the two-tap is selected for this research's proposed pixel, since this is one of the simplest structures. However, as mentioned in Chapter 2.1.2, total 4 outputs per pixel are required for the measurement of depth. Therefore, off-pixel memory is needed for the 2-tap demodulation pixel. Figure 3.1 shows the overall operation of the 2-tap demodulation pixel.

As illustrated in figure 3.1, 2-tap demodulation pixel has only 2 storage nodes, i.e., taps, inside of it, therefore not only the integration of reflected light, but also the readout of pixels must be done in 2 times. Overall, 4 frames will be readout with 2 frames for each integration since 1 modulated light's integration will be demodulated into 2 frames, in-phase and out-phase images.

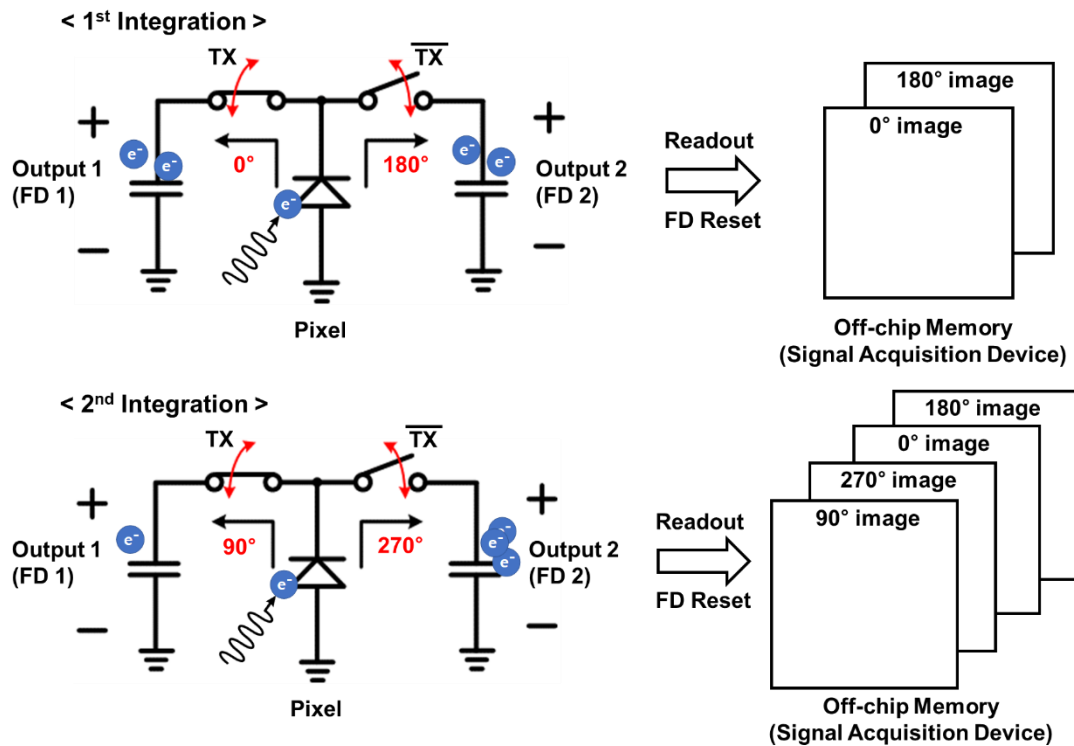


**Figure 3.1** Operation of the 2-tap demodulation pixel with 4-phase signal acquisition. The integration is done 2 times since there are only 2 FD nodes which works as in-pixel memories. In this research, this off-pixel memory is implemented in National Instrument’s signal acquisition device with LabView software.

### 3.1.2 Pull-and-Split Charge Transfer Demodulation Pixel Structure

With the trade-offs described in chapter 2.2, the new pixel design is needed for high resolution depth imaging, and it must have optimal structure, thickness of an epitaxial layer, and a good fill factor. Therefore, the pixel with Pull-and-Split charge transfer is proposed in this research, and it is described in Figure 3.2.

The proposed pixel has pull-and-split charge transfer for demodulation operation. The pixel is implemented using pinned-photodiode structure, and a conventional CMOS image sensor process is used. It is composed of two same photodiodes which are symmetry sideways. Unit photodiode has two n layers which have different n-dose, lower n dose is depicted as PDN1 and higher one as PDN2. Next, the PDN2 area is connected to two TX gates, followed by two FD nodes. It also has two drain nodes, depicted as DX in figure 3.2, which works as anti-blooming operation [12] by draining the electrons inside photodiode onto the pixel’s supply voltage node (VDD in the center of figure 3.2 top).

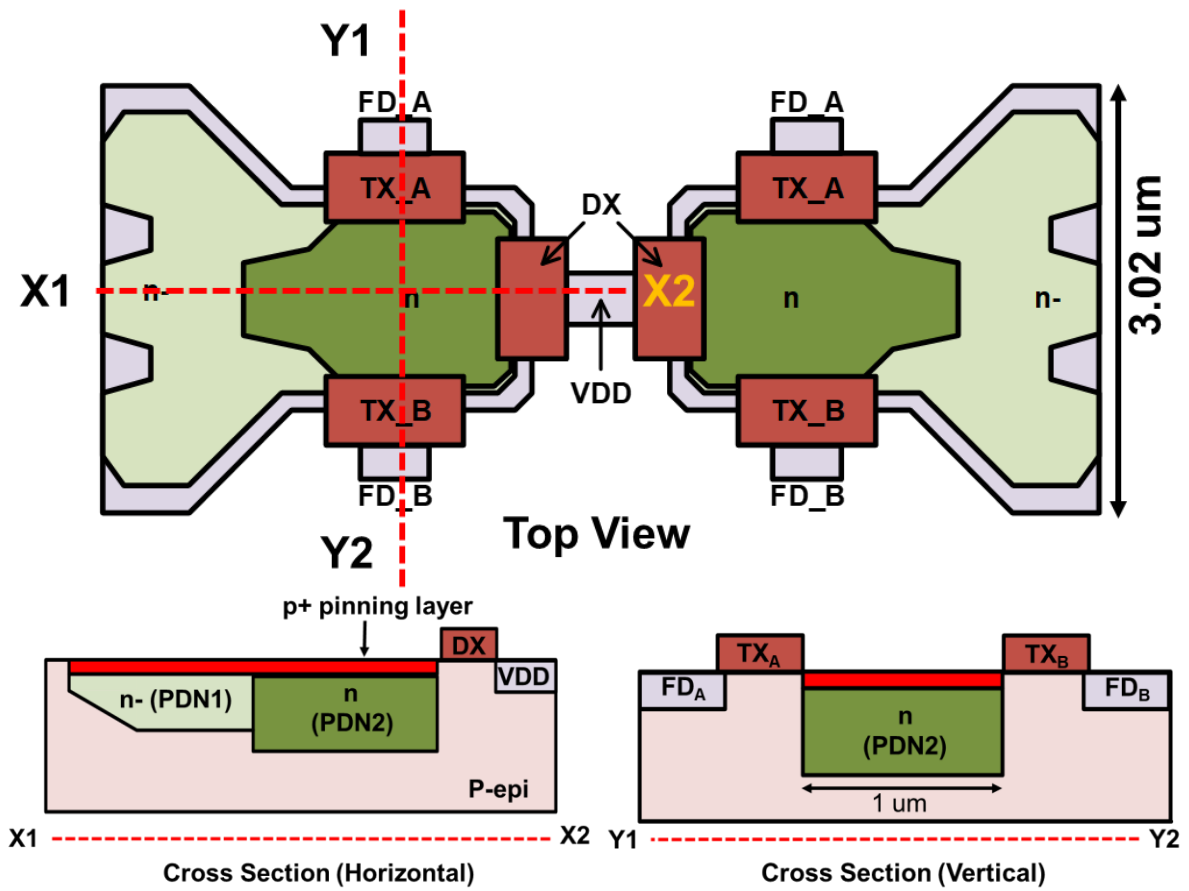


**Figure 3.2** (Top) Proposed pixel structure with Pull-and-Split charge transfer strategy implemented with PPD. (bottom left) Horizontal cross section (X1-X2 direction) of proposed pixel structure. (bottom right) Vertical cross section (Y1-Y2 direction) of proposed pixel structure.

### 3.1.3 Pull Stage Transfer via Pinning Potential Gradient

The important property of pinned photodiode is that the pinning voltage inside PD is changed based on not only each layer's dose implant, but also the n-dose's geometry [5]. First, assuming the same geometry is applied, the higher n-dose has higher pinning potential since the amount of space charge is increased. Next, with the same dose implant, if the area of applied n-dose is small, that part of the PPD will have lower pinning voltage than the other part with a large area of n-dose implant.

With this property, the hexagonal shape of PDN1 is designed to generate regional pinning potential gradient inside the wide area. As for the PDN2 mask, the boundary that PDN1 and PDN2 meets each other is designed with trapezoidal shape. This shape is selected for helping the charge

transfer from PDN1 to the PDN2 area through the pinning potential gradient.

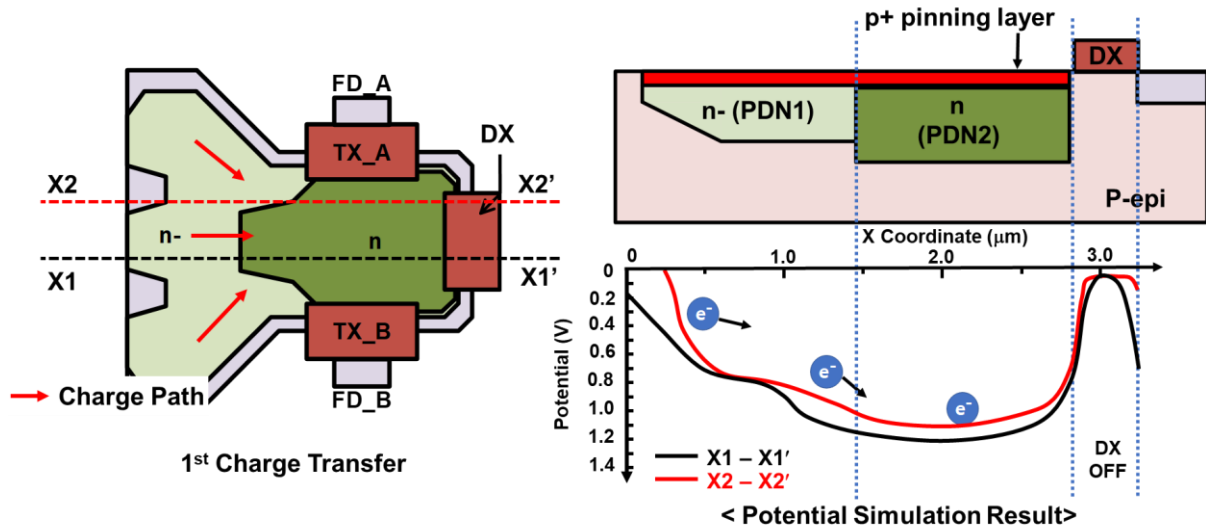


**Figure 3.3** (Top right) Horizontal (X1-X2 direction) cross section of the proposed pixel structure. (bottom right) Simulation of  $V_{pin}$  gradient along X1-X1' (black) and X2-X2' (red)

### 3.1.4 Split Stage Transfer via 2-tap Transfer Gates

TX gates should be placed with short displacement each other. As discussed in Chapter 2, the distance of these gates affects the demodulation performance of the pixel, but the fill factor is decreased due to the blockage of incoming light, reducing depth accuracy. In the proposed pixel, the distance is selected as 1 μm to have high demodulation performance, and the wide PDN1 area supports higher fill factor to keep the signal intensity high enough. If the distance becomes longer in this structure, since PDN2's dose is higher, the potential slope from PD to FD will be decreased, reducing demodulation contrast. If the PDN2 is not applied, the photoelectrons generated in the wide area of PDN will not be transferred in front of TX gates, since the pinning potential in front of TX gates will be lower than a wide area.

In figure 3.4, the split step of charge transfer is simulated with SPECTRA TCAD and is illustrated in 1-D potential profile along vertical (Y1-Y2) direction, and the potential simulation result from top view is drawn in figure 3.5.

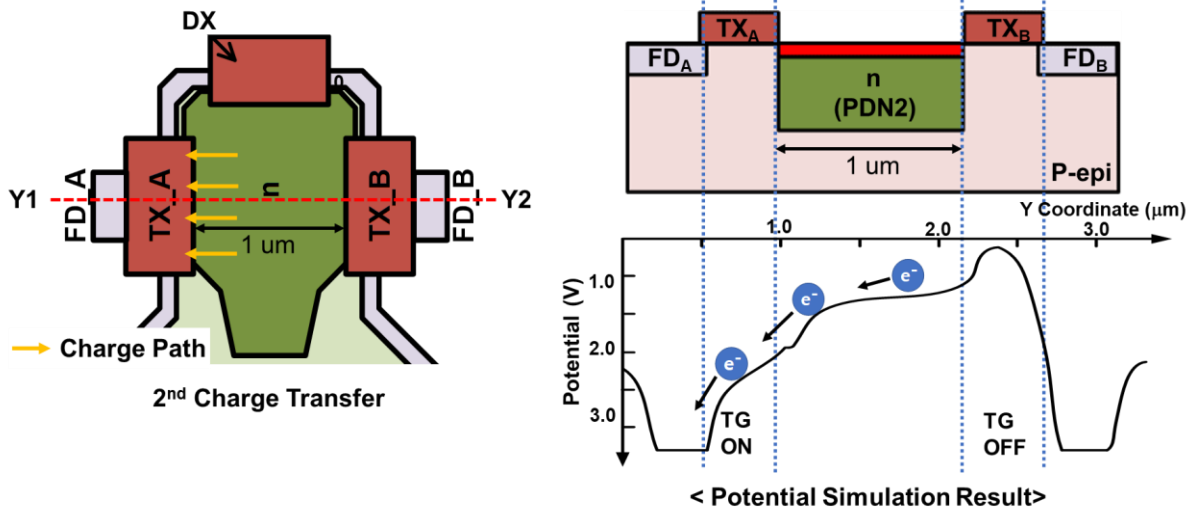


**Figure 3.4** (Top right) Vertical (Y1-Y2 direction) cross section of proposed pixel structure. (bottom right) Simulation of  $V_{pin}$  gradient along Y1-Y2 (black).

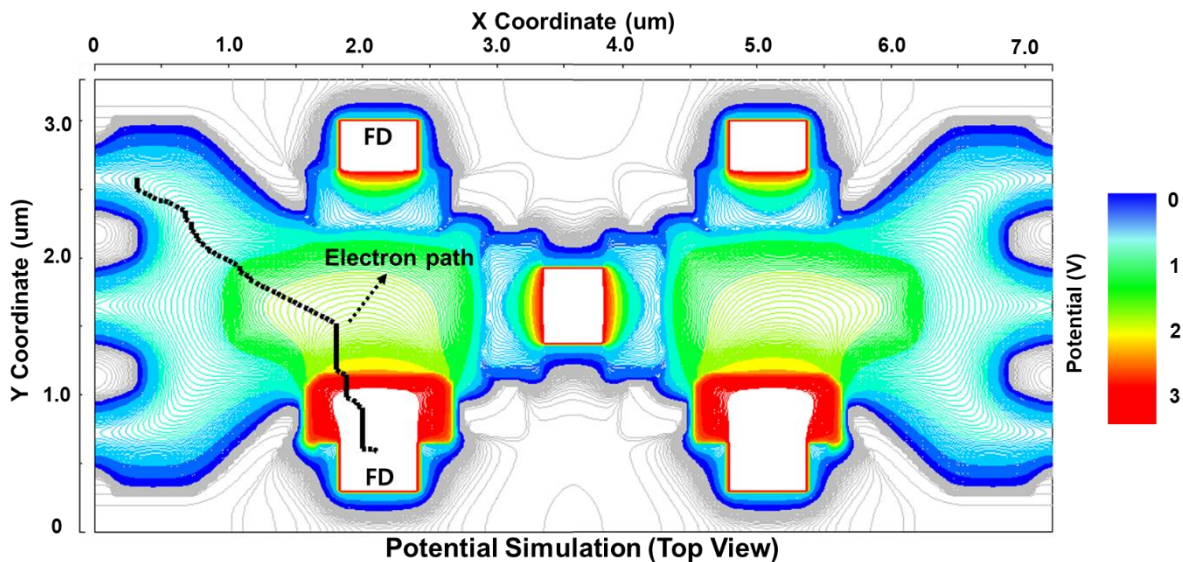


**Figure 3.5** Potential simulation of proposed pixel with top view

### 3.1.5 Demodulation Contrast Improvement using Transfer Gates' $V_{th}$

With the structure of the pixel designed for fast charge transfer while keeping high signal intensity, to improve demodulation contrast even more, the TX gates' threshold voltage must be optimized, otherwise the performance of split step charge transfer will be the bottleneck of demodulation. Therefore, the 4 types of pixel split are implemented with the variation of a deep p-dose implant mask which is used for controlling pinning voltage. Since this dose is implanted before the formation of the poly gate, so it is not self-aligned to the poly gates. Therefore, this implant can

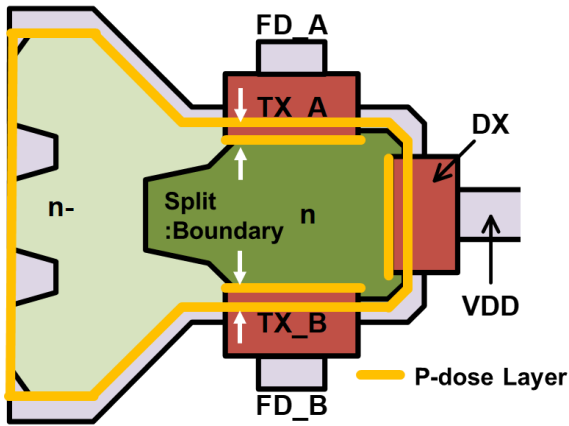


**Figure 3.6** Applied P-dose layer in top view. TXs'  $V_{th}$  is adjusted with the distance from the poly gate.

Name	Split	Details
Split 1	P dose - Poly boundary	High $V_{th}$
Split 2		Mid $V_{th}$
Split 3		Low $V_{th}$
Split 4		NO P-dose Applied

**Table 3.1** The split table of p-dose plan. This was implemented with the mask's distance from the poly gates.

adjust the TX gates' threshold voltage, by applying p-dose under the gate. The illustration of a p-dose layer and its split table is shown in figure 3.6 and table 3.1.

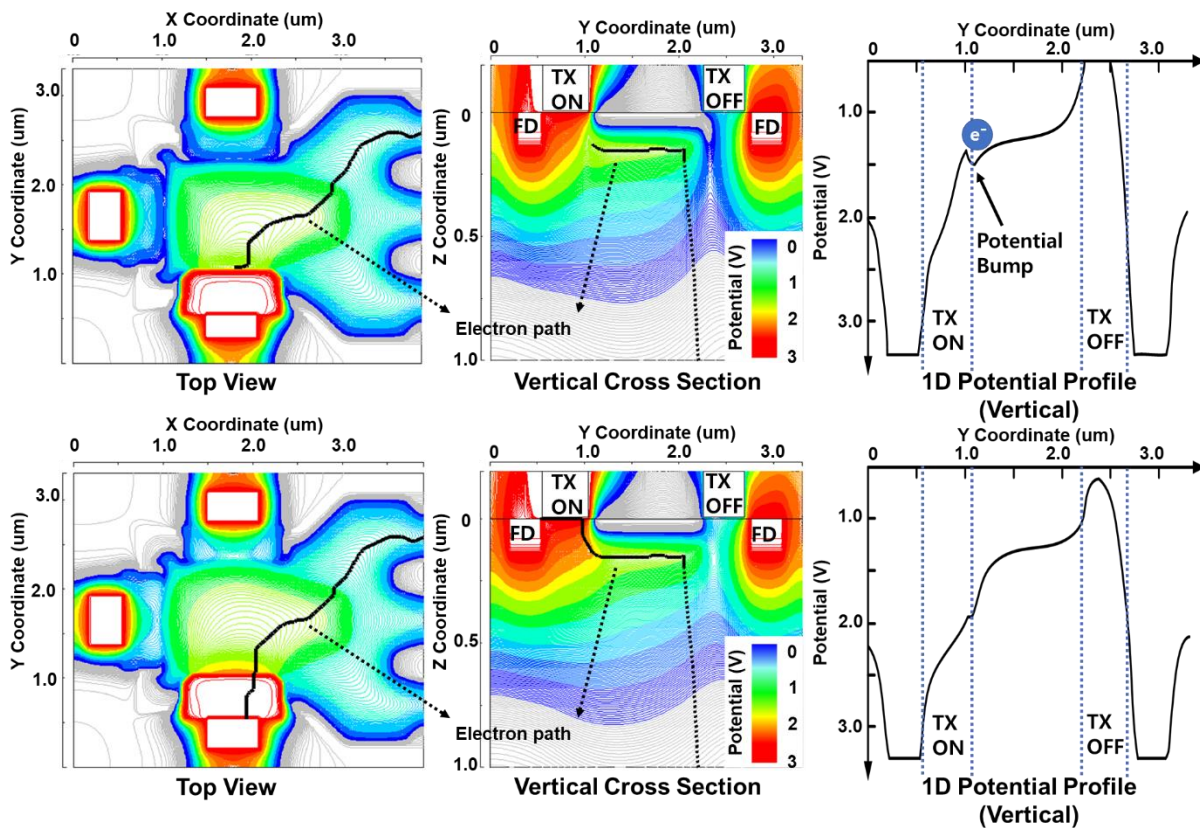


**Figure 3.7** Potential simulation of the proposed pixel with (1<sup>st</sup> column) a top view, (2<sup>nd</sup> column) cross section through vertical direction, (3<sup>rd</sup> row) 1D potential profile along the vertical cross section. Each row in this figure represents from split #1 to split #4, from top to the bottom. Each split's characteristics is described in table 3.1. (Continued to the next page)

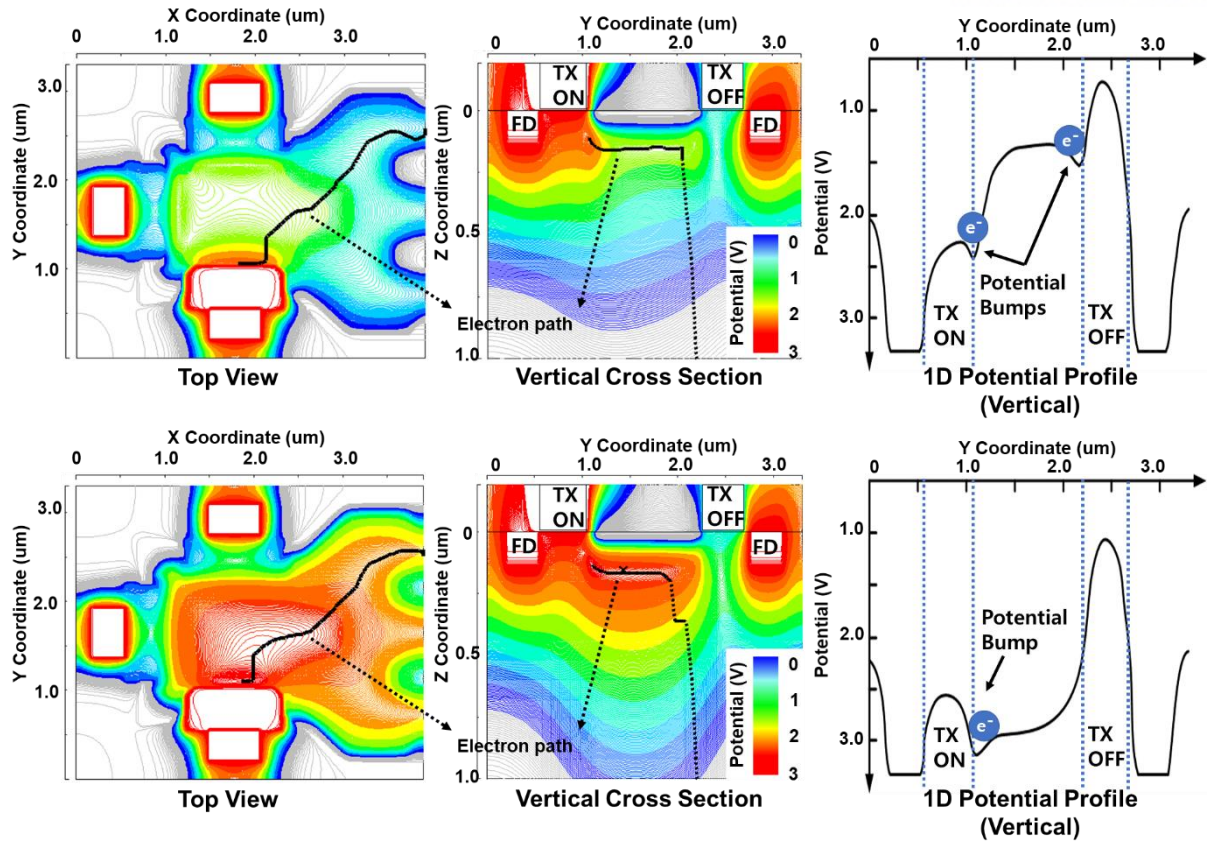


**Figure 3.7** Potential simulation of the proposed pixel with (1st column) a top view, (2nd column) cross section through vertical direction, (3rd row) 1D potential profile along the vertical cross section. Each row in this figure represents from split #1 to split #4, from top to the bottom. Each split's characteristics is described in table 3.1. (Continued from the subsequent page)

From the simulation result depicted in figure 3.6, the vertical cross section of simulation shows that the electron transfer efficiency is optimal at split #2, since for the other splits, the vertical potential profile (the right column of figure 3.6) shows the potential bumps in front of TX gates. These potential bumps may interrupt charge transfer, thus full charge transfer can be interrupted.

## 3.2 Performance Comparison through the Measurement

### 3.2.1 Experiment Setup

For measurement, 3 types of chips with different pixels are implemented with various epitaxial layer thickness by implementing wafer split and n-dose split. First, the wafer split is composed of 3 thicknesses, 3.0um, 6.5um, and 13.5um. Detailed split information is described in table 3.2.

From each of the epitaxial layer thickness, the pixel's demodulation contrast and an overall depth resolution can be observed, and for each epi-thickness, the effect of pinning voltage in the same

pixel can also be observed, thus the optimal epi-thickness and the pinning voltage for the proposed pixel can be found.

As for the pixel structure, with the proposed pixel structure, simple 2-tap demodulation presented in [13] is also fabricated. As discussed in Chapter 2.2.3, the signal's intensity is related to the pixel's optical fill factor. This pixel's structure is composed of 4x4 photodiodes binned into the unit pixel, and each photodiode has two TX gates on left end and right end. Having the photosensitive area between these two TX gates, the drift force generated by the gates directly pulls the electron towards the FD nodes through the gate, thus demodulation function is performed. For comparison with the same functionality, the DX gates are added on top and bottom of this pixel's unit photodiode, thus the fill factor is reduced. This pixel's structure and potential profile are depicted in figure 3.8.

		Thin epi		Mid-epi		Thick epi	
Wafer Number		1	2	3	4	5	6
Epi-Thickness (RS)		3.0um		6.5um		13.5um	
PDN BASE IMP	Base	1	2	3	4	5	6
PDN-1 IMP	$V_{pin1}$			3		5	
	$V_{pin2}$				4		6
	$V_{pin3}$	1					
	$V_{pin4}$		2				
PDN-2 IMP	Base	1	2	3	4	5	6

**Table 3.2** The wafer split for experiment setup. Epi-thickness with 3.0um, 6.5um, and 13.5um is classified as thin, mid, and thick epi wafers, and each epi-thickness have a pinning dose implant split, from  $V_{pin1}$  to  $V_{pin4}$ .  $V_{pin4}$  generates the highest pinning voltage, and  $V_{pin1}$  forms the lowest.



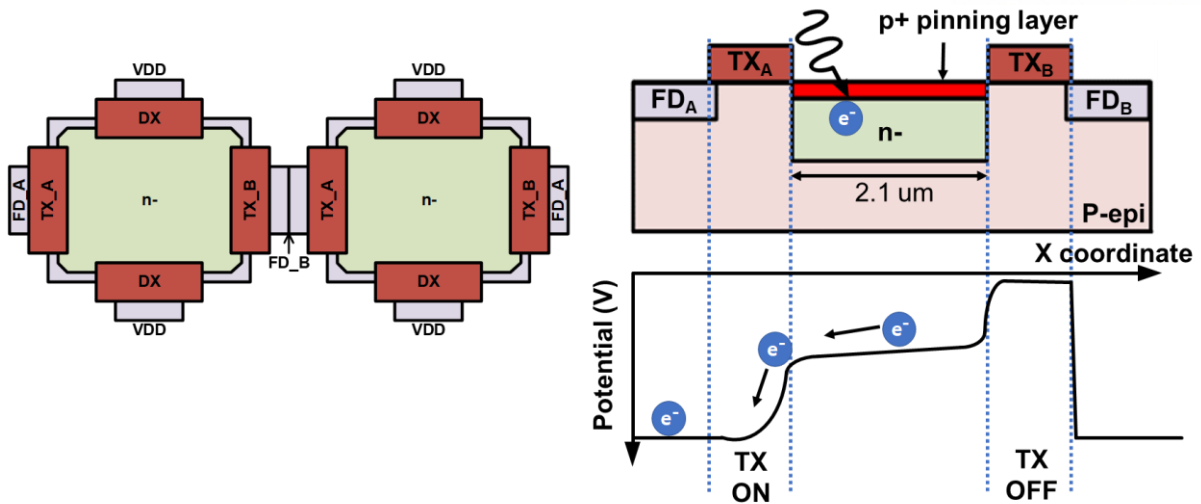


**Figure 3.8** (left) Top view of the conventional 2-tap pixel for performance comparison. (right top) Cross section of the same pixel. (right bottom) The potential diagram of the pixel alongside the cross section [13].

Another chip includes the proposed pixel structure, which contains the pixel splits with the TX gates' threshold voltage (discussed in 3.1.4) is applied. The chip's layout with the pixel splits applied is shown in figure 3.9.

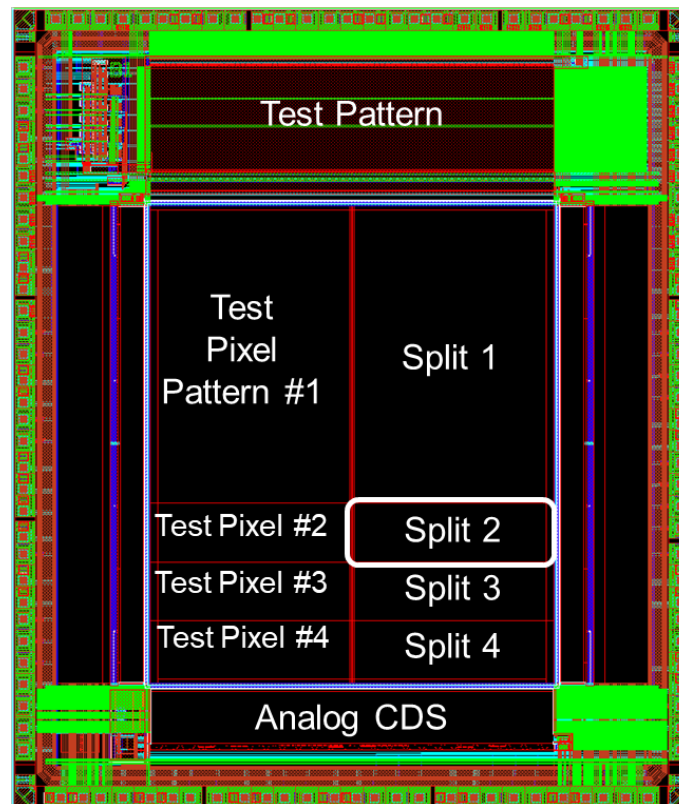


**Figure 3.9** Layout of the full chip with TX gates' threshold voltage split is applied. The Split 2 is highlighted with a white colored box, since this split is measured as optimal TX in simulation.

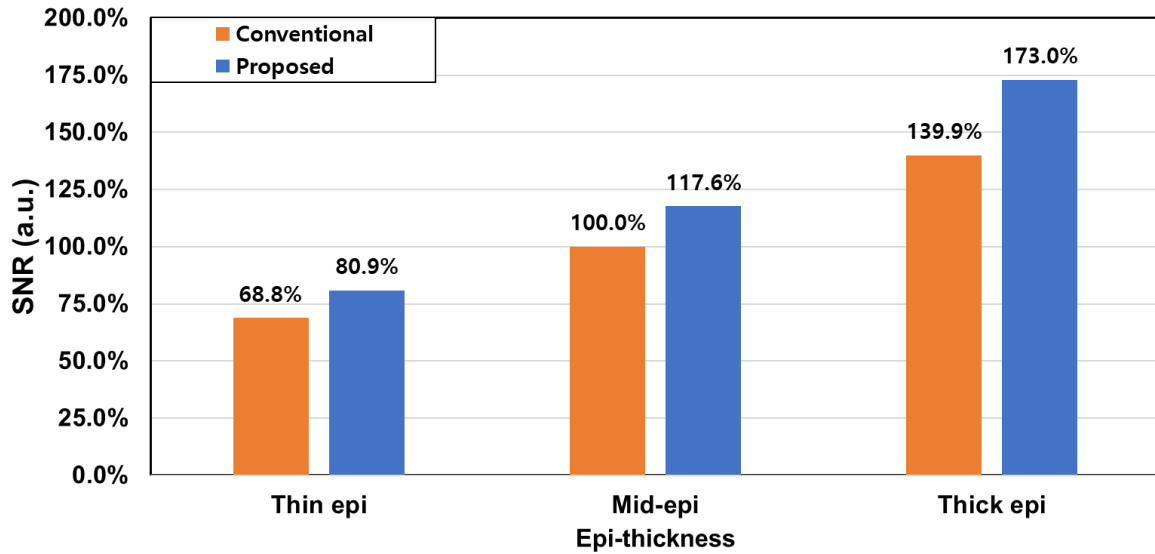


**Figure 3.10** Comparison of SNR between the conventional pixel in [13] and the proposed pixel. The result is plotted with relative value, with the conventional pixel with mid epi thickness as a standard.

### 3.2.2 Signal Intensity Improvement

Comparing the conventional pixel depicted in figure 3.8, the proposed pixel's design has less TX gates in the same area, thus a higher fill factor is expected. To address this improvement, the measurement of the signal intensity with same background light is done. This measurement was done without optical NIR filter and done for all epitaxial layer thickness. The figure 3.10 shows the result that average signal improvement is about 20% for all epitaxial layer cases.

### 3.2.3 Demodulation Contrast of TX Threshold Voltage split

On the left side of figure 3.11, it shows the resultant distance output at a modulation frequency of 25MHz, and the right graph of figure 3.11 shows demodulation contrast of TX Vth splits. From figure 3.11, the result distance is not measured in split #1 and #4. For split #1, potential bumps detected in front of the TX gate, and split #4 showed too high pinning voltage, thus electrons cannot be transferred through the TX gate's potential barrier even the gate is turned on.

Out of expectation was split #3, which does not seem to be working in device simulation, but actual measurement of this pixel gave the proper distance result. Possible reason is that when the electrons transferred via the pinning potential gradient is collected at the PDN2 area first, and the TX gates turn on, even though the potential bump is detected in front of turned-off TX, the potential slope of turned-on TX direction is steeper than those of turned-off TX direction, so most of the photoelectrons are transferred towards to the turned-on TX direction, thus the demodulation is possible.

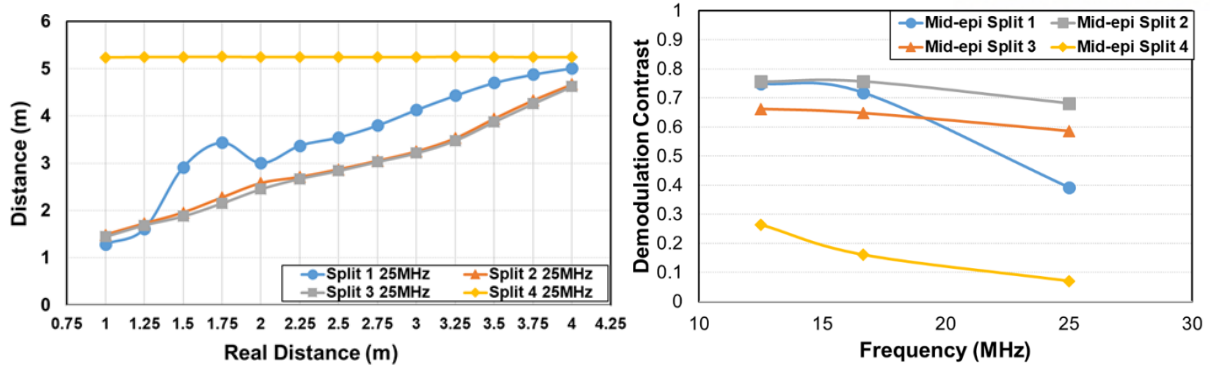


**Figure 3.11** (left) Measured distance result of the TX gate splits. Distance is measured in 25MHz modulation frequency. This result is not calibrated. (right) The demodulation contrast of the TX gate splits. Both measurements were done in the same wafer, mid epitaxial layer.

However, the most promising pixel among the splits is selected to split #2, since the demodulation contrast showed better than split #3, and the depth image showed less pixel variations. Figure 3.12 shows the example of pixel variation.

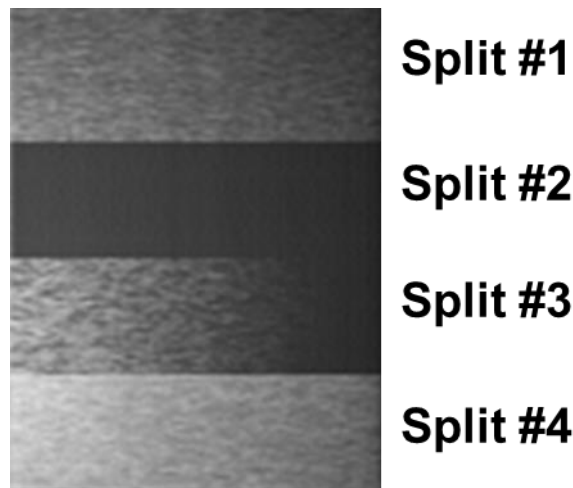


**Figure 3.12** Qualitatively measured pixel variation of each split. The split 2 shows the best performance for pixel-to-pixel variation. The dark side of split 3 shows less pixel variations, proving the effect of the potential bump in front of turned-on TX gate captures electrons.

### 3.2.4 Performance Measurement with Different Epitaxial Thickness

With the best split is fixed to split #2, the performance measurement is done with different modulation frequency. The measured distance result, demodulation contrast, and depth resolution of 1 pixel is discussed here.

First, measured distance output with the different epitaxy layer is shown in figure 3.13. All the epitaxial layer chips with the proposed pixel works as expected. Next, the demodulation contrast with different frequency and epitaxial layer is depicted in figure 3.14. As written, the thinnest epitaxial layer case showed the lowest demodulation contrast, which shows the different result discussed in chapter 2.2.4, however this should be noted that the highest pinning voltage is applied to the thinnest epitaxial layer wafer, and it is depicted in table 3.2. Therefore, the mid epi case and the thick epi case should be compared for analyzing the effect of the epitaxial layer and demodulation contrast.

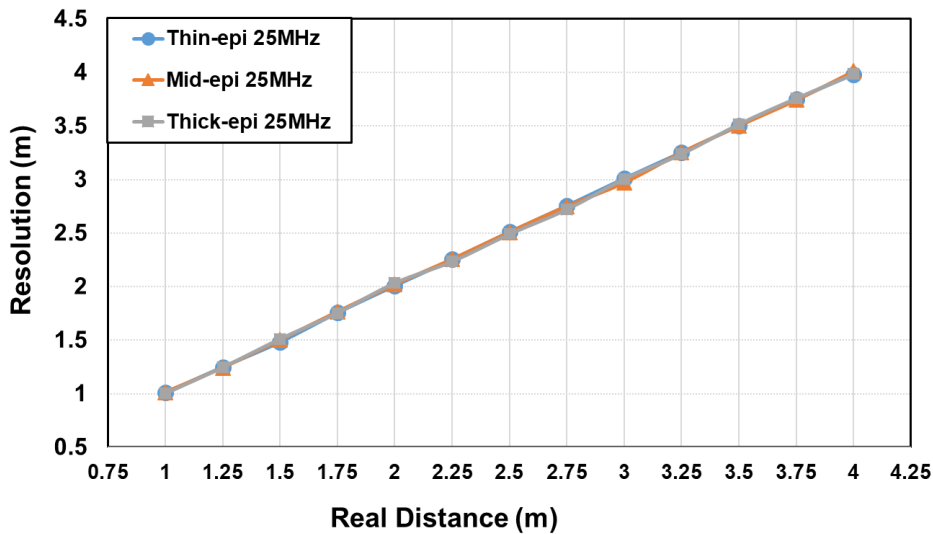


**Figure 3.13** Measured depth output. Measurement is done onto the white colored wall, and the result is 1<sup>st</sup> order calibrated.

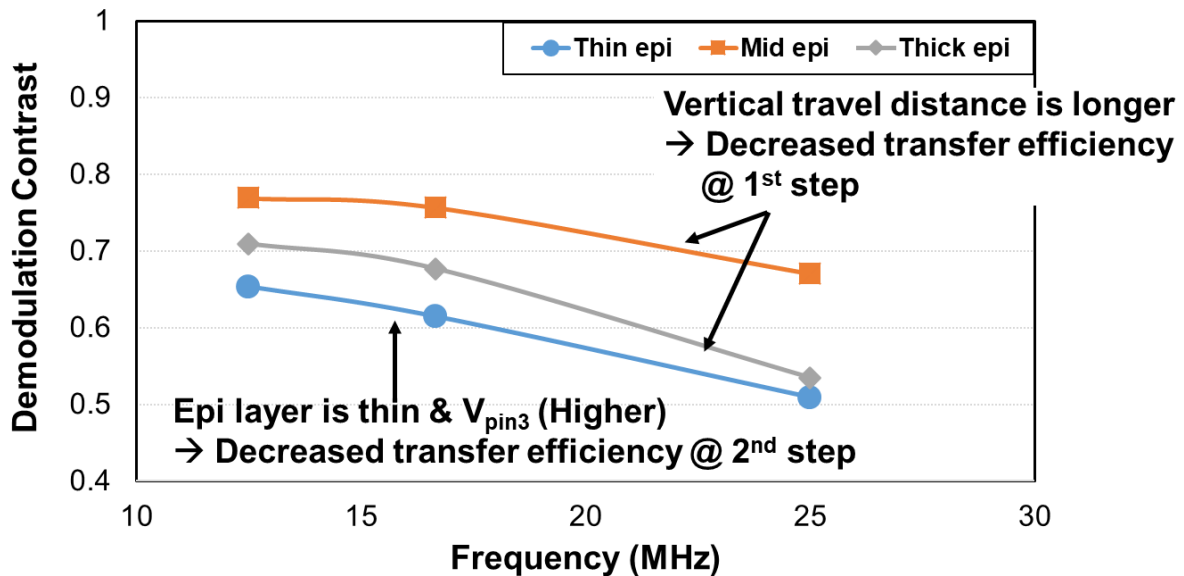


**Figure 3.14** Measured demodulation contrast for different epitaxial layer thickness. The thin epi layer case has lowest demodulation contrast value since it has highest pinning voltage is used, so the potential at the PDN2 area is highest, making the potential slope of split step of charge transfer less efficient.

In figure 3.15, the depth resolution of two cases is compared, lower one (12.5MHz) and the higher one (25MHz) for all epitaxial layer thickness cases. For a 12.5MHz case, the depth resolution result follows the demodulation contrast result for thin and mid epi cases, but the thick epi case has a higher resolution result even though it has lower demodulation contrast according to the measurement of figure 3.14. This result came from the SNR improvement of the epitaxial layer thickness. This trend is continued for a 16.66MHz case (the middle graph of figure 3.15). Next, for a higher modulation frequency case (25MHz), the depth result becomes better for the mid epi case than the thick epi case. Since the demodulation contrast is decreased more at a thick epi case, even though the thick epi has large SNR, the depth result becomes worse. Bottom graph of the figure 3.15 shows this.

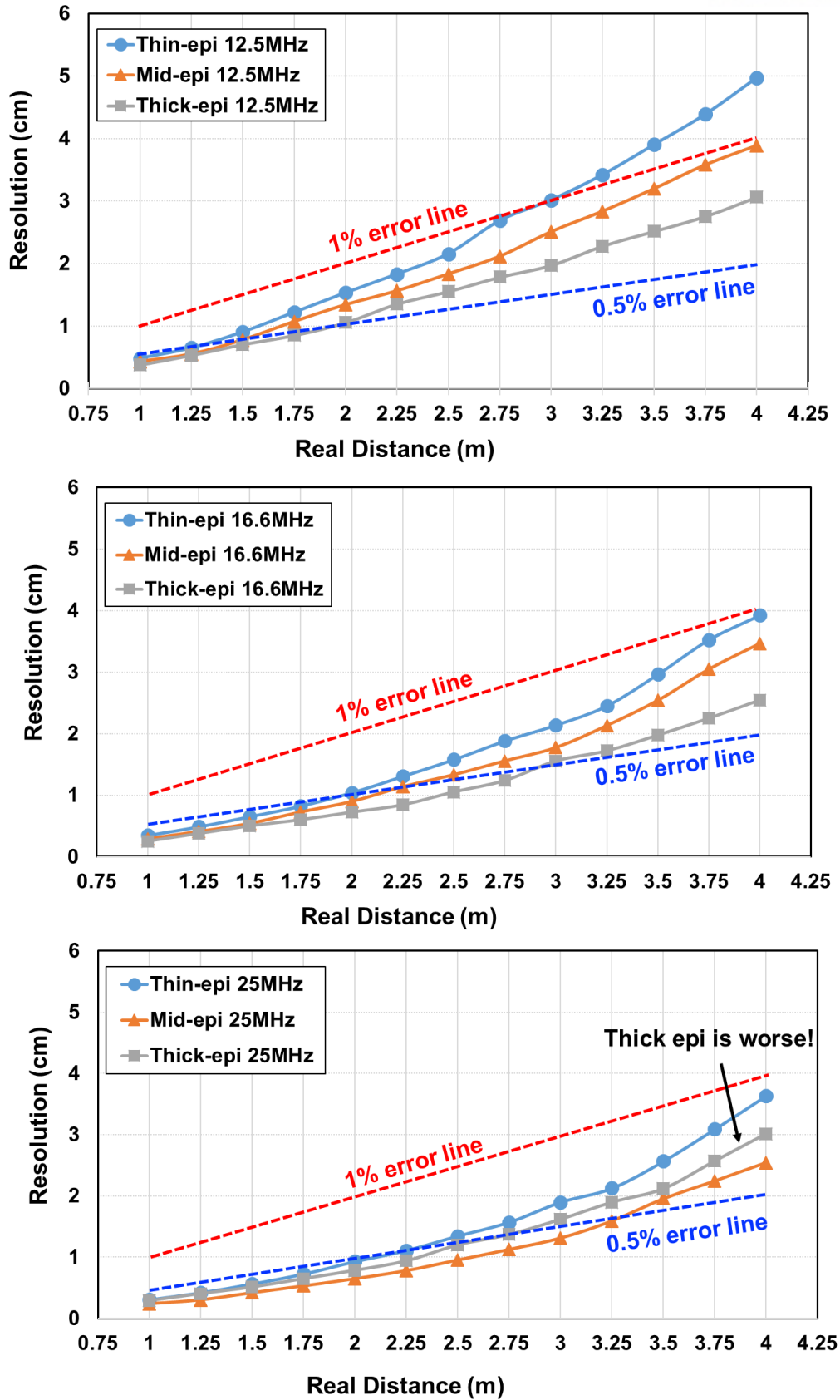


Figure 3.15 Measured depth resolution with different epitaxial layer thickness, (top) at low modulation frequency (12.5MHz). (middle) at 16.66MHz (bottom) at 25MHz.

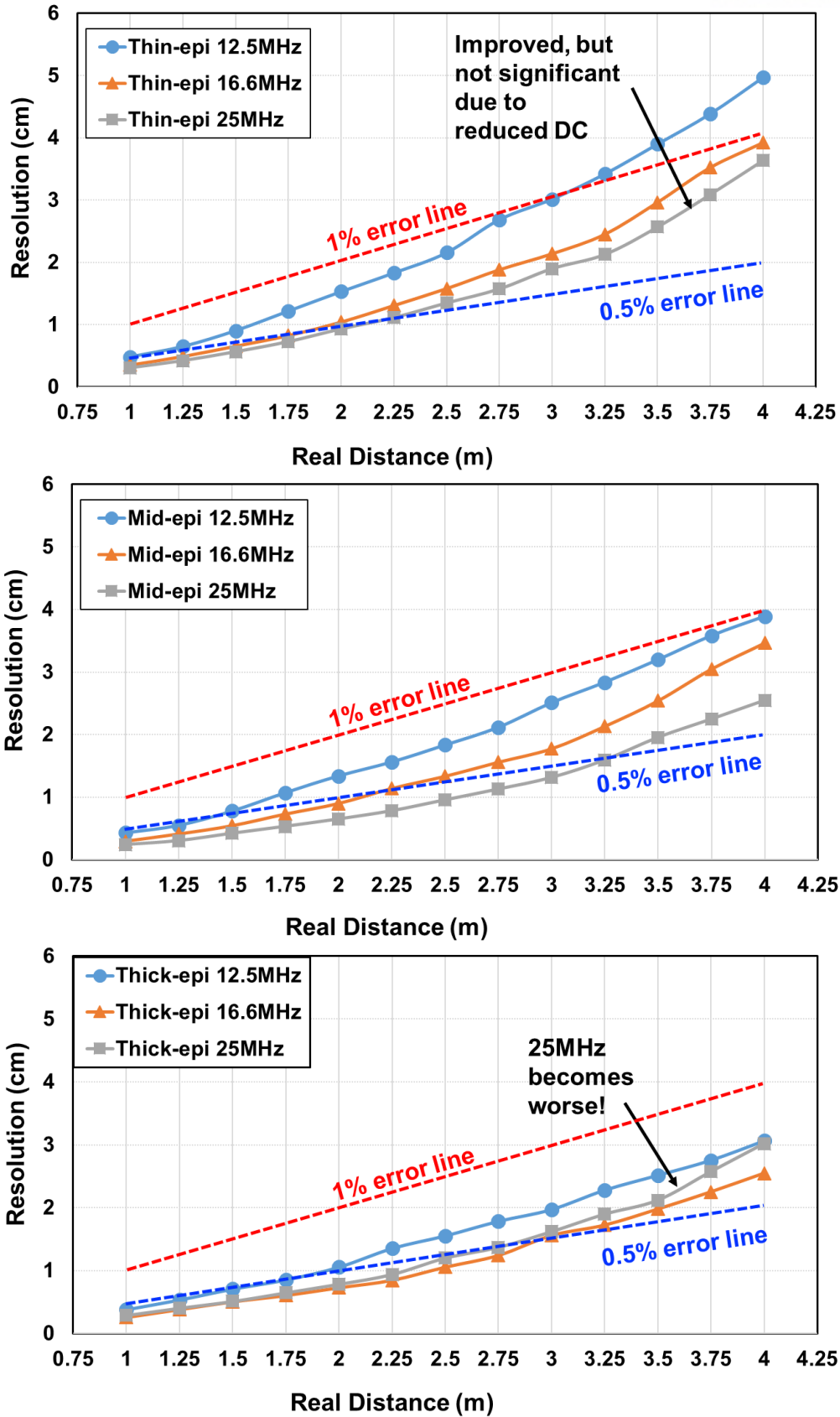
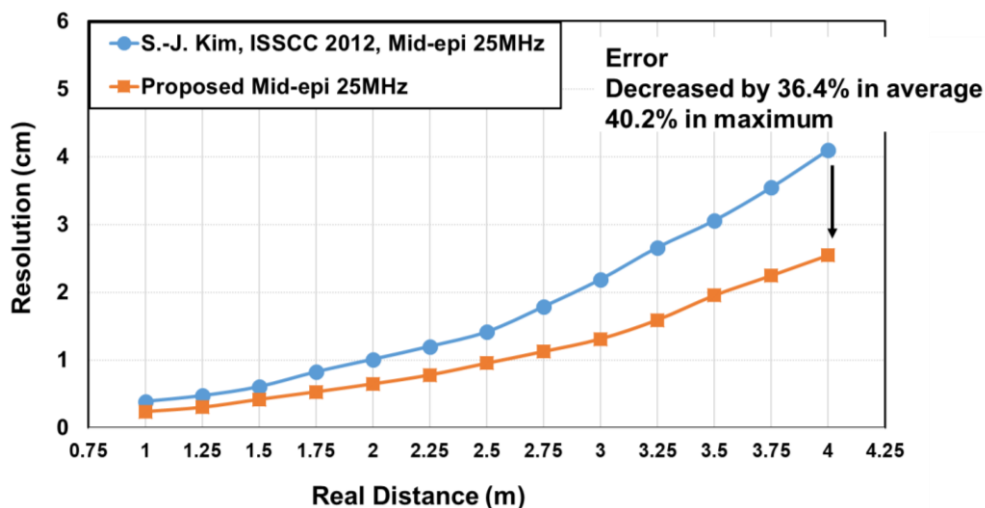


Figure 3.16 Measured depth resolution with different modulation frequency, (top) at thin epi chip, (middle) mid epi chip, (bottom) thick epi chip.

### 3.2.5 Performance Measurement with Different Modulation Frequency

Same measurement done in chapter 3.2.5 is explained in modulation frequency perspective in here. Figure 3.16 shows the comparison of depth resolution with different modulation frequency. Each graph result is fixed to the same epitaxial layer thickness. In thin epi case, since it has low signal intensity and low demodulation contrast, the resolution exceeds 1% error line in low frequency case but is increased in 16.66MHz case. However, from 16.66MHz to 25MHz case, the resolution has not been improved comparing to the amount of increased frequency, due to the decreased demodulation frequency. The mid epi case shows the reasonable depth error improvement pattern since the demodulation contrast has not been decreased much at a higher frequency, so the resolution is improved. For the thick epi case, since the demodulation contrast is decreased from 0.7 at 16.66MHz to 0.52 at 25MHz, the depth resolution becomes worse in a 25MHz case. Overall, the mid epitaxial layer with 25MHz is selected for the best depth resolution performance and is compared with the measurement of conventional pixel's depth resolution, as depicted in figure 3.17.



**Figure 3.17** Measurement of the depth resolution of the conventional pixel is compared with the best performance of the proposed pixel. The error is decreased by 36.4% in average, 40.2% in the maximum.

### 3.2.6 Demodulation Contrast Measurement with Different Pinning Voltage

The demodulation contrast with different pinning voltage is measured in figure 3.18. As for the thin epitaxial layer case, since the vertical directional distance of charge transfer is shortest, the transfer efficiency bottleneck is at the split step of transfer. The low pinning voltage has a steeper potential slope along PDN2 to FD direction, thus the higher e-field is generated. Next, the mid epitaxial layer case shows the trade-off, vertical directional travel distance and potential slope at a



split step transfer, has been cancelled by each other. Therefore, almost similar demodulation contrast is observed. Last, in the thick epitaxial layer case, the vertical transfer became more critical than the other cases, so higher pinning voltage has higher demodulation contrast than the low pinning voltage since high pinning voltage helps the vertical charge transfer, i.e., pull step of charge transfer.

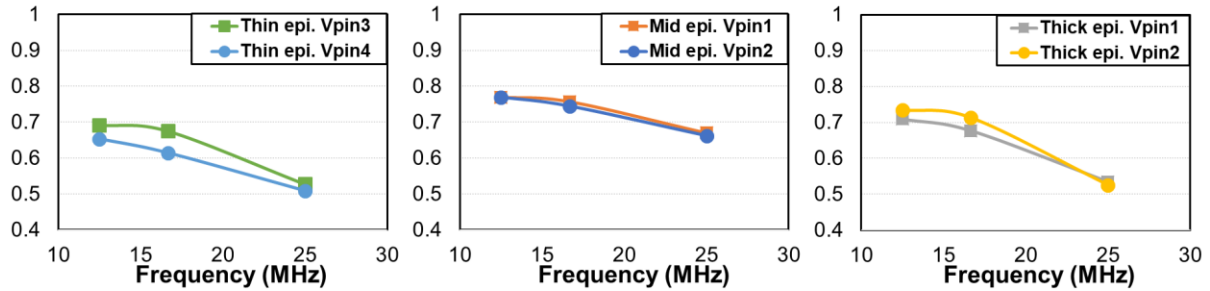


**Figure 3.18** Measured demodulation contrast for (left) the thin epitaxial layer case, (middle) the mid epitaxial layer case, and (right) the thick epitaxial layer case.

---

## Chapter 4. Summary and Future Work

---

In this research, pixel structure for the high depth accuracy implemented with a pinned-photodiode for Indirect Time-of-Flight applications is designed and discussed. The pixel structure takes pull-and-split charge transfer strategy, which can transfer charge fast for efficient demodulation in high modulation frequency, while keeping the signal intensity high enough. Based on the conventional CMOS image sensor process, the trade-offs among the demodulation contrast, optical fill factor, and the threshold voltage of the transfer gates are considered for the design. Through the simulation, optimal p-dose for proper threshold voltage is found and verified the simulation result with actual measurement.

Through the wafer split, the effect of the epitaxial layer and photosensitivity of the pixel is compared and the trade-off between the epitaxial layer thickness and demodulation contrast of the pixel is also measured and discussed. In addition, the relation between demodulation contrast and pinning voltage is measured for each wafer split. Last, the proposed pixel's best depth resolution case, 25MHz operation with mid epitaxial layer thickness is compared to the previous work's pixel, which gave the 40% improvement of resolution.

Although the improvement has been accomplished, since the illumination board is composed of 96 LED arrays, the maximum modulation frequency was limited to 25MHz. The implementation of the new NIR illumination board is needed using laser diodes, or VCSELs for much higher frequency.

	This work	JSSC 2018 [14]	JSSC 2015 [15]
Process	0.11um 1P4M CIS	90nm CIS	TSMC 0.13um 1P5M
Chip size	5.9 mm x 4.85 mm	N/A	8.2 mm x 14.2 mm
Image resolution	200 x 233	320 x 240	512 x 424
Pixel pitch	14.4 um	10 um	10 um
Measured distance	1 ~ 4 m	N/A	0.8 ~ 4.2 m
Maximum Modulation Frequency	25MHz	100MHz with CAPD	130MHz with CAPD
lens	F#1.4, 8mm with NIR Filter	N/A	N/A
Depth resolution	2.8 ~ 25mm (mid-epi) @ 4m White wall	5.9mm @ 1m	< 4mm @ 1m (< 0.5% of range)
Illuminator	96 LED array, 850nm	850 nm	860nm edge emitter laser

	ISSCC 2018 [16]	ISSCC 2014 [17]	J-EDS 2014 [18]
Process	TSMC 65nm BSI 1P8M	TSMC 0.13 1P5M	0.11um 1P4M CIS
Chip size	5.4 mm x 9.8 mm	8.2 mm x 14.2 mm	9 mm x 9.3 mm
Image resolution	1024 x 1024	512 x 424	320 x 240
Pixel pitch	3.5 um	10 um	16.8 um
Measured distance	0.2 ~ 4 m	0.8 ~ 4.2m	0.8 ~ 1.8m
Maximum Modulation Frequency	320MHz with CAPD	130MHz with CAPD	13ns (Light pulse width) 30ns (Gate pulse width)
lens	F# 1.2	F# 1.07	F# 2.0, 12.5mm
Depth resolution	< 1.6mm @ 1m (< 0.2% of range)	< 0.5% of range	5.5 ~ 12.2mm
Illuminator	860 nm	860nm	96 LED array, 870nm

**Table 3.3** Performance comparison table

---

## List of Figures and Tables

---

**Figure 1.1** The triangulation diagram and depth formula. Two observation point are needed, X and Y.

**Figure 1.2** The Michaelson Interferometer. The lights are described in dashed one and solid line, to distinguish two paths of beam-splitter's output.

**Figure 1.3** The Time-of-Flight method diagram. It is composed of IR emitter and detector, and the detector reads the round-trip time of the emitted light.

**Figure 1.4** The comparison of three methods based on target distance and the measurement uncertainty [1].

**Figure 2.1** Basic principle of Indirect Time-of-Flight 3D imaging system.

**Figure 2.2** Sampling of received light in an Indirect Time-of-Flight sensor.

**Figure 2.3** Timing diagram of the same time delay with different modulation frequency.

**Figure 2.4** Timing diagram of demodulation sequence. Demodulating received light and store them on different storage is the key performance for demodulation.

**Figure 2.5** Two pixels which have different fill factor. The size of photosensitive area defines the sensitivity to incoming light, thus gives high SNR.

**Figure 2.6** Large fill factor can have more light signals, but transfer efficiency is decreased. This may cause the decrease of the charge transfer efficiency, decreasing demodulation contrast.

**Figure 2.7** Thicker epitaxial layer may increase photosensitivity of photodiode, especially in longer wavelength. However, since some of the photoelectrons have longer travel distance to reach the destination, FD nodes, and e-field generated by TX gates is much weaker, so charge transfer efficiency is decreased.

**Figure 2.8** Structure of CAPD in [2]. Vguide1 and Vguide2 works as nodes to apply demodulation current, and Vdet1 and Vdet2 are detection nodes.

**Figure 2.9** (left) The structure and (right) the potential diagram of pinned photodiode [3].

**Figure 3.1** Operation of the 2-tap demodulation pixel with 4-phase signal acquisition. The integration is done 2 times since there are only 2 FD nodes which works as in-pixel memories. In this research, this off-pixel memory is implemented in National Instrument's signal acquisition device with LabView software.

**Figure 3.2** (Top) Proposed pixel structure with Pull-and-Split step charge transfer strategy implemented with PPD. (bottom left) Horizontal cross section (X1-X2 direction) of proposed pixel structure. (bottom right) Vertical cross section (Y1-Y2 direction) of proposed pixel structure.

**Figure 3.3** (Top right) Horizontal (X1-X2 direction) cross section of the proposed pixel structure.

(bottom right) Simulation of  $V_{pin}$  gradient along X1-X1' (black) and X2-X2' (red)

**Figure 3.4** (Top right) Vertical (Y1-Y2 direction) cross section of proposed pixel structure.

(bottom right) Simulation of  $V_{pin}$  gradient along Y1-Y2 (black).

**Figure 3.5** Potential simulation of proposed pixel with top view

**Figure 3.6** Applied P-dose layer in top view. TXs'  $V_{th}$  is adjusted with the distance from the poly gate.

**Figure 3.7** Potential simulation of the proposed pixel with (1st column) a top view, (2nd column) cross section through vertical direction, (3rd row) 1D potential profile along the vertical cross section. Each row in this figure represents from split #1 to split #4, from top to the bottom. Each split's characteristics is described in table 3.1. (Continued to the next page)

**Figure 3.8** (left) Top view of the conventional 2-tap pixel for performance comparison. (right top) Cross section of the same pixel. (right bottom) The potential diagram of the pixel alongside the cross section.

**Figure 3.9** Layout of the full chip with TX gates' threshold voltage split is applied. The Split 2 is highlighted with a white colored box, since this split is measured as optimal TX in simulation.

**Figure 3.10** Comparison of SNR between the conventional pixel and the proposed pixel. The result is plotted with relative value, with the conventional pixel with mid epi thickness as a standard.

**Figure 3.11** (left) Measured distance result of the TX gate splits. Distance is measured in 25MHz modulation frequency. This result is not calibrated. (right) The demodulation contrast of the TX gate splits. Both measurements were done in the same wafer, mid epitaxial layer.

**Figure 3.12** Qualitatively measured pixel variation of each split. The split 2 shows the best performance for pixel-to-pixel variation. The dark side of split 3 shows less pixel variations, proving the effect of the potential bump in front of turned-on TX gate captures electrons.

**Figure 3.13** Measured depth output. Measurement is done onto the white colored wall, and the result is 1st order calibrated.

**Figure 3.14** Measured demodulation contrast for different epitaxial layer thickness. The thin epi layer case has lowest demodulation contrast value since it has highest pinning voltage is used, so the potential at the PDN2 area is highest, making the potential slope of split step of charge transfers less efficient.

**Figure 3.15** Measured depth resolution with different epitaxial layer thickness, (top) at low modulation frequency (12.5MHz). (middle) at 16.66MHz (bottom) at 25MHz.

**Figure 3.16** Measured depth resolution with different modulation frequency, (top) at thin epi chip, (middle) mid epi chip, (bottom) thick epi chip.

**Figure 3.17** Measurement of the depth resolution of the conventional pixel is compared with the best performance of the proposed pixel. The error is decreased by 36.4% in average, 40.2% in the maximum.

**Figure 3.18** Measured demodulation contrast for (left) the thin epitaxial layer case, (middle) the mid epitaxial layer case, and (right) the thick epitaxial layer case.

**Table 3.1** The split table of p-dose plan. This was implemented with the mask's distance from the poly gates.

**Table 3.2** The wafer split for experiment setup. Epi-thickness with 3.0um, 6.5um, and 13.5um is classified as thin, mid, and thick epi wafers, and each epi-thickness have pinning dose implant split, from Vpin1 to Vpin4. Vpin4 generates highest pinning voltage, and Vpin1 forms the lowest.

**Table 3.3** Performance comparison table

---

## References

---

- [1] D. Stoppa, L. Pancheri, N. Massari, M. Malfatti, M. Perenzoni, G. Pedretti and G.-F. D. Betta, "Time of Flight Image Sensors in 0.18  $\mu$ CMOS Technology: a Comparative Overview of Different Approaches," *Proceedings of the international image sensor workshop*, p. 2011.
- [2] S. Sze, *Semiconductor devices: physics and technology*, John Wiley & Sons, 2008.
- [3] F. e. a. Acerbi, "Optimization of Pinned Photodiode Pixels for High-speed Time of Flight Applications," *Journal of the Electron Devices Society*, 2018.
- [4] Y. Oike, M. Ikeda and K. Asada, "Smart Access Image Sensors for High-Speed and High-Resolution 3-D Measurement based on Light-Section Method," *Intelligent Automation & Soft Computing*, no. 10, pp. 105-128., 2004.
- [5] R. Schwarte, "Principles of 3-D Imaging Techniques," in *Handbook of Computer Vision and Applications*, Academic Press, 1999, p. 468.
- [6] R. Lange, "3D Time-of-flight distance measurement with custom solid-state image sensors in CMOS/CCD-technology," *Ph.D. Dissertation*, 2000.
- [7] B. Büttgen, T. Oggier, M. Lehmann, R. Kaufmann and F. Lustenberger, "CCD/CMOS Lock-In Pixel for Range Imaging: Challenges, Limitations and State-of-the-Art," *1st range imaging research day*, pp. 21-32, 2005.
- [8] W. S. Boyle and G. E. Smith, "Charge Coupled Semiconductor Devices," *Bell System Technical Journal*, no. 49, pp. 587-593, 1970.
- [9] N. V. Daniel, "Novel standard CMOS detector using majority current for guiding photo-generated electrons towards detecting junctions," *Proceedings Symposium IEEE/LEOS Benelux*, pp. 229-232, 2005.
- [10] N. Teranishi, "No image lag photodiode structure in the interline CCD image sensor," *International Electron Devices Meeting*, pp. 324-327, 1982.
- [11] N. Teranishi, "Effect and limitation of pinned photodiode," *IEEE Transactions on Electron Devices*, no. 63, pp. 10-15, 2015.
- [12] S. Kawahito, I. A. Halin, T. Ushinaga, T. Sawada, M. Homma and Y. Maeda, "A CMOS Time-of-Flight Range Image Sensor With Gates-on-Field-Oxide Structure," *IEEE Sensors Journal*, pp. 1578-1586, 2007.
- [13] S.-J. Kim, B. Kang, J. D. K. Kim, K. Lee, C.-Y. Kim and K. Kim, "A 1920 $\times$ 1080 3.65 $\mu$ m-Pixel 2D/3D Image Sensor with Split and Binning Pixel Structure in 0.11 $\mu$ m Standard CMOS," *ISSCC Dig. Tech. Papers*, pp. 396-398, 2012.
- [14] Y. Kato, T. Sano, Y. Moriyama, S. Maeda, T. Yamazaki, A. Nose, K. Shiina, Y. Yasu, W. v. d.

- Tempel, A. Ercan, Y. Ebiko, D. V. Nieuwenhove and S. Sukegawa, "320×240 Back-Illuminated 10- $\mu$ m CAPD Pixels for High-Speed Modulation Time-of-Flight CMOS Image Sensor," *IEEE Journal of Solid-state Circuits*, vol. 53, no. 4, pp. 1071-1078, 2018.
- [15] C. S. e. a. Bamji, "A 0.13 $\mu$ m CMOS System-on-Chip for a 512 × 424 Time-of-Flight Image Sensor With Multi-Frequency Photo-Demodulation up to 130 MHz and 2 GS/s ADC," *IEEE Journal of Solid-State Circuits*, vol. 50, no. 1, pp. 303-319, 2015.
- [16] e. a. Cyrus S. Bamji, "1Mpixel 65nm BSI 320MHz Demodulated TOF Image Sensor with 3.5 $\mu$ m Global Shutter Pixels and Analog Binning," *ISSCC*, pp. 94-96, International Solid-State Circuits Conference.
- [17] e. a. Andrew Payne, "A 512×424 CMOS 3D Time-of-Flight Image Sensor with Multi-Frequency Photo-Demodulation up to 130MHz and 2GS/s ADC," *IEEE International Solid-State Circuits Conference*, pp. 134-136, 2014.
- [18] S.-M. e. a. Han, "A time-of-flight range image sensor with background canceling lock-in pixels based on lateral electric field charge modulation," *IEEE Journal of the Electron Devices Society*, pp. 267-275, 2014.